# TEAD1 condensates are transcriptionally inactive storage sites on the pericentromeric heterochromatin

Jindayi Liang[1,7,10], Yiran Wang[1,10], Justin Demmerle[1,8], Britney Jiayu He[1,9], Christopher J. Ricketts[2], W. Marston Linehan[2], Chongzhi Zang[3,4], Danfeng Cai[1,5,6,11*]

[1]Department of Biochemistry and Molecular Biology, Johns Hopkins Bloomberg School of Public Health, Baltimore, Maryland

[2]Urologic Oncology Branch, National Cancer Institute, Bethesda, Maryland

[3]Department of Genome Sciences, University of Virginia, Charlottesville, Virginia

[4]University of Virginia Comprehensive Cancer Center, University of Virginia, Charlottesville, Virginia

[5]Department of Biophysics and Biophysical Chemistry, Johns Hopkins School of Medicine, Baltimore, Maryland

[6]Department of Oncology, Johns Hopkins School of Medicine, Baltimore, Maryland

[7]Present address: California Institute of Technology, Pasadena, California

[8]Present address: Cancer Research Center, Fralin Biomedical Research Institute, Virginia Tech, Washington DC

[9]Present address: Scripps Research Institute, San Diego, California

[10]These authors contributed equally

[11]Lead contact

*Correspondence: D. Cai (danfeng.cai@jhu.edu)

**Abstract**

TEA domain transcription factor 1 (TEAD1), a Hippo pathway transcription factor important in cellular homeostasis and development, is increasingly implicated in cancer biology. Here, we reveal a novel role for TEAD1 in organizing nuclear condensates, independent of active transcription. Using high-resolution imaging, ChIP-seq, RNA-seq and proximity-based proteomics, we demonstrate that in patient-derived renal cell carcinoma cells, TEAD1 forms micron-sized foci by binding to the heterochromatic pericentromeric regions using its DNA-binding domain. These TEAD1 foci do not mediate transcription but instead serve as depots for excess TEAD1. This contrasts with TEAD1 organization in other genomic regions of both RCC and normal kidney cells, where TEAD1 associates with markers of active transcription. Our findings provide a mechanistic framework for TEAD1's dual regulatory roles, offering new insights into its contribution to transcriptional dysregulation and tumor progression.

## Introduction

Key nuclear processes such as transcription, RNA splicing, and DNA repair occur in membrane-less compartments known as biomolecular condensates[1-3]. These condensates are broadly defined as dynamic assemblies formed through weak interactions between proteins and nucleic acids[1,2,4]. Transcriptional condensates, specifically, are formed by transcription-related factors[5]. Although they have garnered increasing attention, their mechanisms of formation and function remain poorly understood. While liquid–liquid phase separation is the dominant model explaining their assembly[6,7], alternative mechanisms—such as low-valency interactions with spatially clustered DNA binding sites—have also been proposed[8,9]. Moreover, although transcriptional condensates are generally associated with promoting gene expression[10-12], some have been shown to repress transcription[13,14]. Thus, a deeper understanding of how transcriptional condensates form and function in biologically relevant contexts is essential, particularly for developing strategies to target them in diseases like neurodegeneration and cancer[15,16].

Renal cell carcinoma (RCC) is a common type of kidney cancer. While there have been considerable improvements in disease-free survival among patients with RCC, effectively managing metastatic disease continues to be a significant challenge in clinical practice, and a clear understanding of the molecular mechanism of RCC progression is still much needed[17]. Genetic alterations in RCC frequently occur in the Hippo pathway[18], a deeply conserved signaling network regulating cell growth[19]. The Hippo pathway includes key proteins such as STE20-like kinase 1/2 (MST1/2), large tumor suppressor kinase 1/2 (LATS1/2), scaffold proteins such as Salvador homologue 1 (SAV1), and neurofibromatosis type 2 (NF2), which can be activated by cell-cell contacts[20]. The main role of the Hippo pathway is to phosphorylate and repress its downstream transcriptional coactivators, Yes-associated protein (YAP), or its homolog, transcriptional coactivator with PDZ-binding motif (TAZ), by sequestration in the cytoplasm[21-23]. Therefore, when the Hippo pathway is off or mutated such as in RCC (most mutations occur in

NF2 or Sav1[18,24]), YAP/TAZ translocates into the nucleus, binds to its transcription factor TEA domain 1-4 (TEAD1-4) family proteins, and activates genes promoting cell proliferation and survival[25]. However, where and how the Hippo pathway components are activated inside the cell are not well understood.

Recently, many components of the Hippo pathway have been found to form biomolecular condensates. The two transcription coactivators, YAP and TAZ, were first discovered to form condensates that activate transcription[4,10,26]. Subsequently, upstream Hippo pathway kinases and adaptor proteins were also observed to form condensates with varying pathway activation or repression outcomes[27,28]. While it has been shown by us and other labs that transcription factors TEAD1-4 can incorporate into YAP and TAZ condensates[4,10,26], TEAD1-4 have not been found to form condensates by themselves. Additionally, the specific functions of Hippo pathway components condensates in various cancers are unknown.

In this study, we focus on transcription condensates formed by TEA domain family member 1 (TEAD1) in Hippo pathway-mutated RCC. We found that, different from most other transcription condensates, TEAD1 foci localize to the heterochromatin in the pericentromeric regions, and do not mediate active transcription. Our combined ChIP-seq/RNA-seq analysis and proteomics data suggest that TEAD1 foci may be a storage site for buffering excessive TEAD1 such as in Hippo-negative kidney cancer cells. These results reveal an interesting alternative function for transcription condensates and new ways cells can harness condensates in homeostasis and diseases.

**Results**

We aimed to determine if YAP or TEAD proteins form biomolecular condensates in cancer cells, especially those with high YAP or TEAD expression. Therefore, we examined a previously

established diverse panel of patient-derived renal-cell carcinoma (RCC) cells, the UOK cell lines[29]. Among these lines, UOK121, UOK122, UOK139, and UOK140 are clear cell RCC lines, and UOK275 and UOK342 are papillary RCC lines. A non-cancerous kidney tubule cell line, HK2, was used as a control. Since phase separation and condensate formation are tightly coupled to protein expression levels[1], we first checked the levels of YAP and TEAD1 in these cell lines. We found that HK2, UOK121, UOK342, UOK122, and UOK140 expressed high levels of YAP (**Figs. 1A-B**). Among these cell lines, UOK121 and UOK342 also expressed high levels of TEAD1 (**Figs. 1A-B**). Examining these cell lines for YAP/TEAD1 condensate formation, we found that while YAP is diffusely distributed in the nucleus and cytoplasm in different cell lines (**Supp. Fig. 1F**), TEAD1 forms prominent micron-sized foci only in TEAD1-high UOK121 and UOK342 cells (**Fig. 1C**). We observed at least one, and up to five TEAD1 foci per nucleus in the majority of both UOK121 and UOK342 cells (**Fig. 1D**), most of which were close to either the nuclear lamina or the nucleolus (**Fig. 1E-F**). These are not artifacts from immunofluorescence (IF), as TEAD1 knockdown by RNA interference (RNAi, **Supp. Fig. 1A-B**) eliminated TEAD1 foci (**Supp. Fig. 1C**), nor are they protein aggregates as they did not stain positively for an amyloid marker AmyTracker (**Supp. Fig. 1D**)[30]. Among other members of the TEAD family, TEAD2 and TEAD3 do not form foci, while TEAD4 does form foci, although less prominently, in UOK121 and UOK342 cell lines (**Supp. Fig. 1E).** We have previously found that TEAD1 cannot form condensates by itself but can incorporate into YAP condensates and stabilize YAP condensate formation[10,30]. However, finding TEAD1 foci in the absence of YAP condensates is novel (**Supp. Figs. 1F-G**). We were intrigued by these TEAD1 foci and went on to examine how they form and function.

To probe the biophysical properties of TEAD1 foci, we employed fluorescence recovery after photobleaching (FRAP). Specifically, we used full-foci FRAP to examine the diffusion of TEAD1 molecules between TEAD1 foci and the nucleoplasm, and half-foci FRAP to examine the dynamics of TEAD1 inside the foci. We found that TEAD1 foci recovered fluorescence rapidly

after full-foci FRAP, indicating that TEAD1 exchanges quickly between the nucleoplasm and the foci (**Fig. 1G, 1H left**). In half-foci FRAP experiments, the bleached area also recovered fluorescence rapidly (**Fig. 1G, 1H right, blue line**), accompanied by a 25% dip in the unbleached area immediately after bleaching (**Fig. 1H right, magenta line**). These findings indicate that TEAD1 molecules preferentially mix within TEAD1 foci, consistent with an LLPS-driven mechanism[8]. Treatment with 1,6-hexanediol (1,6HD), an aliphatic alcohol[1,2,31] , on the other hand, did not dissolve the TEAD1 foci in the nucleus nor did it alter their number (**Fig. 1I-J**). Together, these results all indicate that TEAD1 foci are liquid-like compartments stabilized by interactions that are not primarily hydrophobic.

**TEAD1 foci do not mediate active transcription.**

TEAD family transcription factors usually mediate active gene expression. To investigate if TEAD1 foci also mediate active transcription, we examined their association with RNA polymerase II phosphor-Serine2 (RNA Pol II-pSer2), a marker of transcription elongation[32], H3K27 acetylation (H3K27ac) — a histone modification denoting active enhancers[33], and Bromodomain-containing protein 4 (BRD4) — a transcriptional coactivator found at super-enhancers[34,35]. To our surprise, TEAD1 foci did not colocalize with any of these active transcription markers but instead excluded them (**Figs. 2A-G**). Furthermore, TEAD1 foci did not colocalize with the canonical YAP/TEAD target gene *CYR61* (also called *CCN1*) when visualized by simultaneous IF against TEAD1 and nascent RNA-FISH against *CYR61* (**Figs. 2H-K**). These results indicate that TEAD1 foci do not mediate active transcription at YAP/TEAD1 canonical target genes. In addition, TEAD1 foci did not colocalize with other known nuclear membrane-less organelles (MLOs) such as Cajal bodies (**Supp. Figs. 2A, 2D**), nuclear speckles (**Supp. Figs. 2B, 2D**), or PML bodies (**Supp. Figs. 2C, 2D**). TEAD1 foci therefore represent a unique kind of condensate that contains a transcription factor yet does not mediate active transcription.

**TEAD1 foci localize to the pericentromeric heterochromatin region.**

Since TEAD1 foci do not associate with markers of active transcription (**Figs. 2A-G**) and are close to the nuclear lamina and the nucleolus (**Figs. 1E-F**), regions typically enriched in heterochromatin, we went on to test if TEAD1 foci localize to the heterochromatin itself. Histone 3 lysine 9 trimethylation (H3K9me3) is an epigenetic marker characteristic of heterochromatin[36]. Co-staining of TEAD1 and H3K9me3 showed that every TEAD1 focus colocalizes with an H3K9me3 domain in the TEAD1 foci-positive cell lines UOK342 and UOK121 (**Figs. 3A-D**). No co-occupancy between TEAD1 and H3K9me3 was observed in the TEAD1 foci-negative UOK122 or HK2 cells (**Supp. Figs. 3A-D**). In addition, in UOK121 cells, TEAD1 foci also colocalize with heterochromatin protein 1 alpha (HP1α, **Supp. Figs. 3E-F**), a protein responsible for heterochromatin assembly[37]. Importantly, the heterochromatin regions that TEAD1 foci localize to are always adjacent to the centromere (**Figs. 3E-H, Supp. Figs. 3G-J**), indicating that TEAD1 foci specifically bind to the pericentromeric heterochromatin, a region crucial for centromere integrity and proper segregation of chromosomes during mitosis[38,39]. This is further supported by the much closer distance of TEAD1 foci to the centromere histone marker centromere-specific protein A (CENP-A, 0.2 μm)[38] than the telomere marker telomeric repeat binding factor 2 (TRF-2, 1 μm, **Figs. 3I-L**)[40]. These results indicate that TEAD1 foci specifically localize to the pericentromeric heterochromatin.

**TEAD1 foci are seeded by DNA Binding**

The localization of TEAD1 foci to the pericentromeric region suggests that TEAD1 foci formation may be seeded by DNA binding. To test this possibility, we constructed mutants of TEAD1 that do not bind to the DNA. The DNA-binding domain of TEAD1 (TEA domain) is a highly conserved region containing three α-helices (H1, H2, and H3) assembled into a homeodomain to interact with the DNA[41] (**Fig. 4A**). We first deleted a region in the TEA domain encompassing H2 and H3 (TEAD1Δ55-122) previously shown to bind to the DNA (**Fig. 4A**)[42]. We expressed this construct

fused with EGFP in both foci-positive and foci-negative cell lines. We found that compared to EGFP-TEAD1, which formed TEAD1 foci co-occupant with the heterochromatin in all cell lines (**Figs. 4B,F,G and Supp. Figs. 4F,J,K**), EGFP-TEAD1Δ55-122 did not form foci in any cells (**Figs. 4C, Supp. Fig. 4G**). However, this mutant also did not concentrate in the nucleus due to the deletion of a nuclear localization signal[43] (**Fig. 4A, underlined**). To disrupt TEAD1 DNA binding specifically without interfering with their nuclear localization, we created point mutations in the H1 (F43P and L47P, TEAD1H1Mut) and H3 (Q89S and S92P, TEAD1H3Mut) helices (**Fig. 4A**) previously shown to disrupt DNA binding[42]. When transiently expressed in both foci-positive and negative cells, we found that although TEAD1H1Mut and TEAD1H3Mut concentrated in the nucleus, they formed fewer and smaller foci (**Figs. 4D-E, Supp Figs. 4H-I**) under similar or even higher expression levels compared to wildtype EGFP-TEAD1 (**Supp. Figs. 4A-E**). In addition, the GFP signal of these mutants did not colocalize with heterochromatin (**Figs. 4F-G, Supp Figs. 4J-K**). These data indicate that the DNA-binding domain of TEAD1 is essential for TEAD1 foci formation on the heterochromatin.

**TEAD1 and YAP co-occupy distal enhancer sites to upregulate gene expression.**

To understand the functions of TEAD1 in regions both outside of and inside of TEAD1 foci, we set out to determine the binding sites of TEAD1 on the genome and investigate their relations to gene expression. To achieve this, we performed chromatin immunoprecipitation followed by sequencing (ChIP-seq) using antibodies against endogenous TEAD1, YAP, H3K27ac, and H3K9me3 proteins, as well as RNA sequencing (RNA-seq), in both TEAD1 foci-positive (UOK121, UOK342) and foci-negative (UOK122, HK2) cell lines. TEAD1 and YAP are known to co-occupy distal enhancer sites in various stem cells and cancer cells[44-46]. Consistent with these results, we found that in all cell lines, most TEAD1 peaks mapped to either distal intergenic (41.9%) or intronic regions (46.7%), while few (5.2%) were found at promoters (**Fig. 5A**). Specifically, over 50% of TEAD1-bound regions were 50kb away from a TSS in UOK121 and UOK342 (**Figs. 5B-C**). Alignment of these

distal TEAD1-bound sites with H3K27ac peaks revealed a bimodal distribution of H3K27ac centered on TEAD1 peaks (**Fig. 5D**). These results indicate that most TEAD1 binds to distal enhancer sites. Not surprisingly, TEAD family-specific MCAT elements[47] are the most enriched binding motifs in regions bound by TEAD1 (**Fig. 5E**). These regions were enriched for Gene Ontology terms such as actin cytoskeleton organization and cell junction assembly (**Fig. 5F**), which are typical YAP/TEAD1-regulated pathways. As expected, TEAD1 and YAP peaks colocalize at canonical TEAD1/YAP target genes such as *CTGF* and *CYR61* (**Fig. 5G**). Combining ChIP-seq and RNA-seq data, we found that the majority of YAP/TEAD1 co-bound regions have upregulated gene expression (**Supp. Figs. 5A-D**). This supports previous reports that the main function of YAP-associated TEAD1 is to activate downstream gene expression.

**TEAD1 foci are intergenic, unique to each cell line, and do not regulate transcription.**

Having confirmed that TEAD1 binds to and activates canonical YAP/TEAD1 target genes, we went on to examine the genomic locations of TEAD1 foci. The pericentromeric regions are known to be highly repetitive[48,49], preventing the exact pinpointing of TEAD1 binding sites to these regions using canonical genomic methods. To overcome this, we first identified H3K9me3 domains using the SICER2 algorithm[50], and then intersected these H3K9me3 domains with TEAD1 binding peaks to identify the binding sites of TEAD1 foci. We found that only a small portion of the total TEAD1 binding sites intersected with the H3K9me3 regions (**Supp. Fig. 5E**). Notably, among these sites, approximately 60% of the TEAD1 peaks localize to distal intergenic regions which extend beyond 500kb from the TSS (**Figs. 5H-I**), indicating that TEAD1 foci may be transcriptionally inactive. TEAD1/H3K9me3 co-bound regions in foci-positive cells (**Fig. 5J**) show greater occupancy of TEAD1 in their respective cell lines, compared to both the other foci-containing line and control lines. This suggests that TEAD1 binding is enriched at these TEAD1 foci in UOK121 and UOK342 cells, contributing to the observed signal in our imaging data. However, these binding sites are not universally shared between the two cell lines. When

comparing the TEAD1 binding peak intensity across the TEAD1-H3K9me3 co-bound regions, we noticed differential enrichments between UOK121 and UOK342, indicating that TEAD1 foci-associated regions can be cell line–specific (**Fig. 5J**). Interestingly, we also observed low levels of TEAD1 binding at these sites even in foci-negative cell lines (**Fig. 5J, Supp. Fig. 5F**), suggesting that TEAD1 localization to heterochromatin can be a general feature across cell types, and that interaction with H3K9me3 is necessary but not sufficient in driving TEAD1 foci formation. In conclusion, TEAD1 binding sites at TEAD1 foci-associated regions can be specific and unique among cell lines.

To examine the roles of TEAD1 foci in gene expression, we performed differential expression analysis of the RNA-seq data comparing foci-positive cell lines (UOK121 and UOK342) with the foci-negative HK2 kidney cell line (**Supp Figs. 5A-B**)[51]. We then performed binding and expression target analysis (BETA)[52] to see if upregulated or downregulated genes are associated with TEAD1-H3K9me3 binding. Interestingly, we found that genes proximal to TEAD1/H3K9me3 co-bound regions were neither upregulated nor downregulated (**Supp Figs. 5G-H**). These results indicate that peri-centromeric TEAD1 foci do not directly regulate transcription and may be a passive storage site for TEAD1 that are overexpressed in these kidney cancer cell lines.

**TEAD1 foci selectively incorporate protein components.**

To further understand the functions of TEAD1 foci, we set out to identify protein components of TEAD1 foci using proximity labeling mass spectrometry[53,54] with UOK342 cells stably expressing miniTurbo-TEAD1-HaloTag (**Fig. 6A**): miniTurbo is a compact biotin ligase for rapid labeling of TEAD1-surrounding proteins with biotin[53], and HaloTag is for visualizing TEAD1 localization with Halo dyes. UOK342 cells expressing miniTurbo-TEAD1 H3Mut-HaloTag, which form no or fewer foci (**Fig. 6B**), were used as controls. We first used imaging to confirm the efficient labeling of TEAD1 foci proteins after 10 minutes of biotin addition, showing colocalization of biotin signal with

TEAD1 signal in both WT and H3mut TEAD1 (**Fig. 6B**). We then enriched the biotinylated proteins from the whole cell lysate using streptavidin beads and confirmed that protein biotinylation increased upon biotin addition (**Supp. Figs. 6A-B**). Using mass spectrometry, we identified a total of 1060 proteins in WT and H3Mut samples (87 unique in WT, 139 unique in H3Mut, with 834 shared between WT and H3Mut, **Supp. Fig. 6C**). We narrowed down the protein list to only those containing biotinylated peptides[55], identifying 13 proteins unique to WT TEAD1, 23 unique to TEAD1 H3Mut, and 69 shared in both conditions (**Figs. 6C-D**). In addition, we compared the differential enrichment of biotinylated peptides in WT TEAD1 with the H3Mut and identified 10 proteins significantly enriched in WT TEAD1, and 6 proteins significantly enriched in H3Mut (**Fig. 6D, $p < 0.05$, 2-fold enrichment**). Gene set enrichment analysis (GSEA) of the enriched and unique proteins in TEAD1 foci revealed nuclear proteins associated with chromatin/chromosome binding and transcriptional regulation, consistent with TEAD1's nuclear functions (**Fig. 6E, Supp Fig. 6D**). GSEA also showed functions in chromatin remodeling and negative regulation of transcription (**Fig. 6E, Supp Fig. 6D**), consistent with our observation that TEAD1 foci localize to the heterochromatin and do not mediate active transcription. Using Co-IF, we confirmed the colocalization of endogenous TEAD4 and HMGB2 (High Mobility Group Box Protein 2, a protein maintaining chromatin structure) with TEAD1 foci in UOK342 (**Figs. 6F-G**). These results indicate that TEAD1 foci selectively incorporate proteins to maintain chromatin structure.

## Discussion

In this study, we identify a novel kind of condensate formed by the transcription factor TEAD1 in RCC cells. Interestingly, these liquid-like TEAD1 foci localize to heterochromatin regions. While their cellular function remains mysterious, we speculate that they represent storage or accumulation sites for excess TEAD1 protein at a relatively harmless genomic location. Cells need to maintain the optimal concentration of their proteins at homeostasis. Insufficient protein amount can lead to delayed entry into mitosis[56,57], while excess proteins can lead to protein

aggregation and/or hyperactivation of downstream signaling[58,59]. Additionally, aberrant activation of oncogenes in non-transformed cells often induces oncogene-induced senescence involving cell cycle arrest[60-62]. Cells achieve protein homeostasis via the regulation of transcription, translation, and protein degradation systems. We propose that protein condensation by TEAD1 can be an efficient way to buffer and limit the damaging effects caused by excess proteins, which may confer survival advantages to RCC cells. In RCC cells, YAP/TAZ and TEAD1 can activate genes mediating ferroptosis, an iron-dependent cell death pathway[63,64]. It is possible that preventing excessive TEAD1 activity by forming TEAD1 foci could protect cancer cells from ferroptosis. On the other hand, not all phenomena in cancer cells are promoting cancer. TEAD1 foci may instead represent a futile attempt of these cells to prevent tumorigenesis by decreasing YAP/TEAD-mediated cell proliferation. Future studies could involve specific modulation of TEAD1 foci to examine their roles in cellular fitness and cancer progression.

It is intriguing that TEAD1 foci do not form at random locations in the nucleus, but instead localize to pericentromeric heterochromatin regions, long considered a transcriptionally inactive region critical for maintaining centromere integrity and proper segregation of chromosomes during mitosis[38,39]. While most transcription factors are absent from those areas, a few examples do exist. Heat shock transcription factor 1 (HSF1) binds to the pericentromeric region of the human chromosome 9 during heat shock, transcribes satellite III repeats there, and forms nuclear stress granules containing HSF1[65,66]. These HSF1 granules are thought to sequester active transcription complexes, such as mammalian CREB-binding protein (CBP), to shut down global transcription during heat shock[67]. Another transcription factor that localizes to the pericentromeric regions is GAGA factor, which binds to the GA/CT repeats and establishes chromatin boundaries in cooperation with Polycomb proteins and the inner nuclear membrane[68,69]. Ikaros is a protein that localizes to the centromeric heterochromatin of lymphocytes, forms foci, and represses nearby genes[70]. Here we propose a novel role of the pericentromeric region, which is to serve as a

reservoir for excess TEAD1 in a DNA-binding dependent manner. Indeed, when we overexpress TEAD1 in other foci-negative cell lines, we observe that TEAD1 foci at heterochromatin are likely to be pericentromeric (**Figs. 3E-H**), indicating that this is a general mechanism utilized by cells to store TEAD1 irrespective of whether the cells are cancerous. This raises the question of whether other important transcription factors can also localize specifically to pericentromeric or other heterochromatic regions and form foci, and if so, what are the functions of these foci?

Recently, condensate-targeting therapies have emerged as a promising way to treat previously untreatable diseases such as neurodegeneration and cancer[15,71-73]. Our data on TEAD1 foci in RCC reveal that not all the condensates observed in diseases are capable of driving that disease. In addition, a single transcription factor can also form condensates of different sizes and locations in different cell types[15]. Therefore, careful studies of condensate morphology and function are paramount for designing precise condensate-targeting treatments.

**Acknowledgements**

We appreciate the discussions and feedback from Anthony Leung and Cai lab members, and the centromere DNA-FISH probe gifted from Alan Meeker. This work is supported by the Department of Defense Kidney Cancer Idea Development Award (W81XWH2210900, D.C.) and the National Institutes of Health (R35GM142837, D.C.; NIH R35GM133712, C.Z.; and intramural grant, W.M.L.).

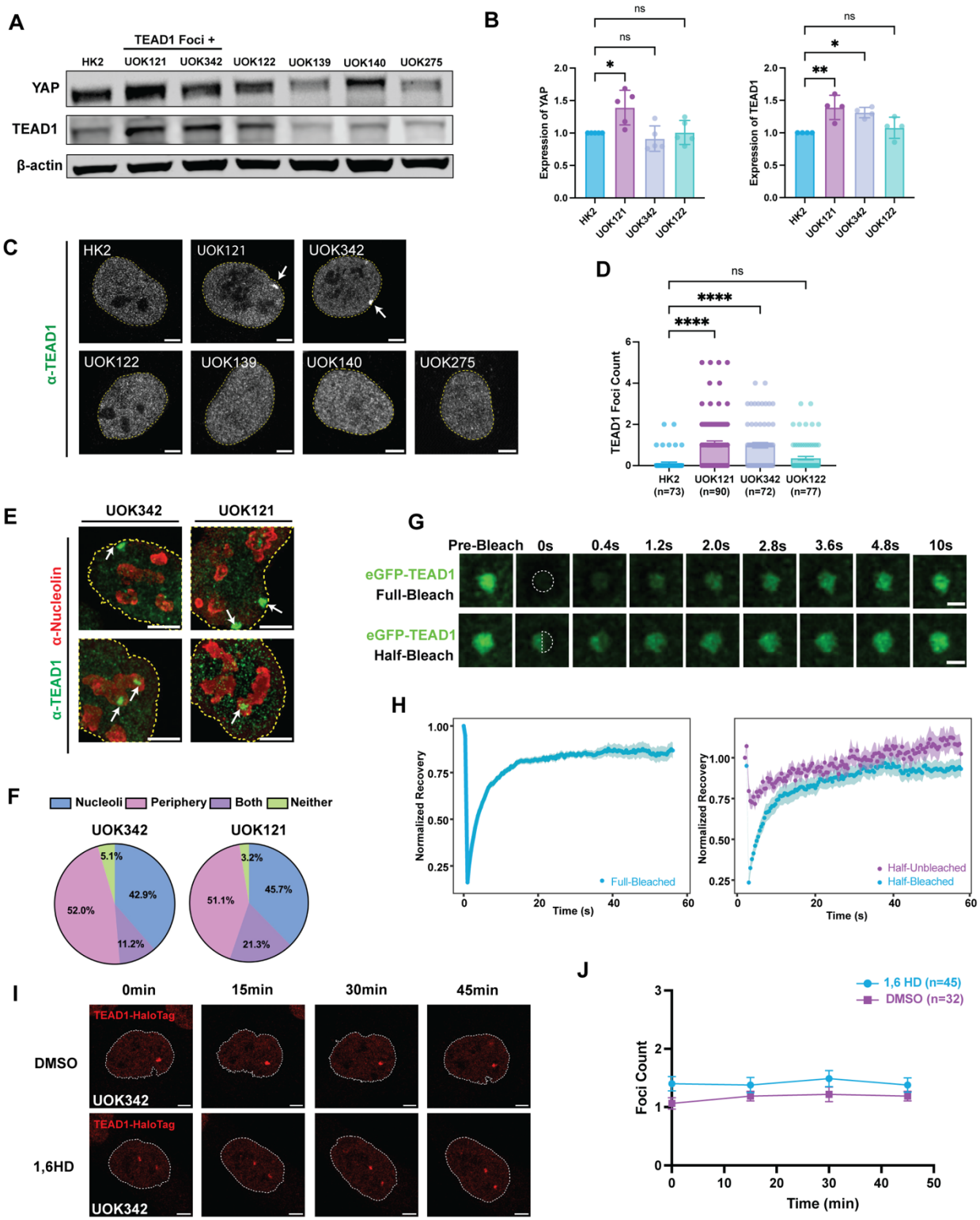


**Figure 1. TEAD1 forms foci in various RCC lines.**

**(A)** Representative immunoblot showing TEAD1 and YAP1 protein levels in TEAD1 foci-positive versus TEAD1 foci-negative cell lines.

**(B)** Quantification of TEAD1 and YAP1 bands from **(A)**, normalized to loading control. Data are presented as mean ± SD.

(C) Immunofluorescence imaging demonstrating TEAD1 foci formation in kidney tubule and renal carcinoma cell lines. Arrows indicate the TEAD1 foci. Scale bar = 5 μm. Nuclear boundaries are indicated by dotted lines.

**(D)** Quantification of TEAD1 foci in UOK121, UOK122, UOK342, and HK2 cell lines using 3D analysis. Data are presented as mean ± SEM.

**(E-F)** Maximum intensity projection from 3D images of TEAD1 (green) and Nucleolin (red) co-immunofluorescence in UOK342 and UOK121 **(E),** with quantification of TEAD1 foci nucleolar and perinuclear localization (n= 94-98 cells) **(F)**.

**(G)** Full-bleach (top) Fluorescence Recovery after Photobleaching (FRAP) and half-bleach FRAP (bottom) of eGFP-TEAD1 UOK342 stable cell line over 10s. Scale bar = 2 μm

**(H)** Quantification of recovered fluorescence intensity of fully bleached TEAD1 foci (left, blue), half-bleached region (right, blue), and unbleached region (right, magenta). Shaded areas indicate the standard error of the mean (SEM) for each measurement (n = 10).

**(I)** Representative live-cell image of UOK342 TEAD1–HaloTag knock-in cells after treatment with DMSO control (top) or 1,6-hexanediol (1,6HD, bottom). HaloTag fluorescence was labeled with JF549 dye. Scale bar = 5 μm.

**(J)** Quantification of TEAD1 foci per cell in **(I)** (n = 45 for 1,6-hexanediol; n = 32 for DMSO). Data are shown as mean ± SEM; error bars represent the standard error of the mean. Statistical significance of all data was determined by one-way ANOVA: ns, $p > 0.05$; **, $p \leq 0.005$; ****, $p \leq 0.0001$.

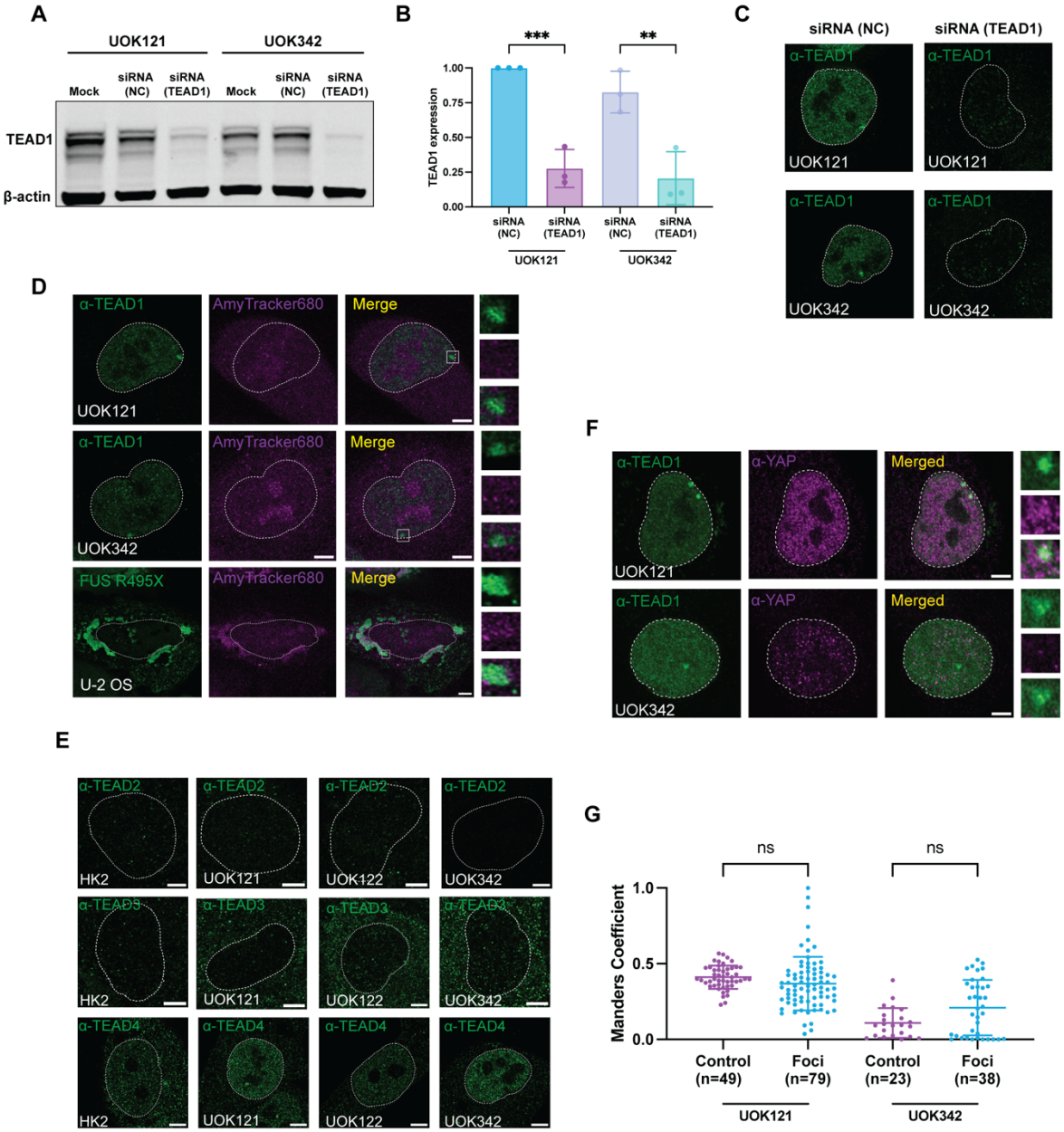


**Supplemental Fig. 1. TEAD1 foci are not protein aggregates or artifacts.**

**(A-B)** Immunoblotting of efficient TEAD1 knockdown in UOK121 and UOK342 cells in **(A),** Mock: no transfection. Quantification of TEAD1 expression between TEAD1 siRNA treatment and negative control (NC) in UOK121 and UOK342 in **(B)**.

**(C)** Immunofluorescence images of TEAD1 (green) in UOK121 and UOK342 cells upon treatment with TEAD1 knockdown siRNA (TEAD1) or control siRNA (NC). Scale bars represent 5 μm. Nuclear boundaries are indicated by dotted lines.

**(D)** Representative 2D immunofluorescence images showing AmyTrakcer680 staining do not overlap with TEAD1 foci visualized by TEAD1 antibody, but overlaps with protein aggregates

formed by expressing FUS R495X mutant (detected by Myc antibody) in U-2 OS cells. Insets show magnified images of boxed regions**.** Scale bars are 5μm. Nuclear boundaries are indicated by dotted lines.

**(E)** Representative 2D immunofluorescence images showing TEAD2-4 staining in HK2, UOK121, UOK342, and UOK122 cells. Scale bars are 5μm. Nuclear boundaries are indicated by dotted lines.

**(F**) Representative immunofluorescence images of TEAD1 foci and their spatial relationship with YAP in UOK121 and UOK342. Insets show magnified images of boxed regions. Scale bars are 5μm. Nuclear boundaries are indicated by dotted lines.

**(G)** Quantitative analysis and statistical evaluation of TEAD1 foci co-localization with YAP staining. Co-localization was assessed using Manders' coefficient within defined regions surrounding TEAD1 foci, with control measurements taken from random nucleoplasmic regions. Data are presented as scatter plots with mean ± SD.

All data are shown as mean ± SD. Statistical significance was determined by one-way ANOVA: ns, $p > 0.05$; **, $p \leq 0.005$; ***, $p \leq 0.0005$.

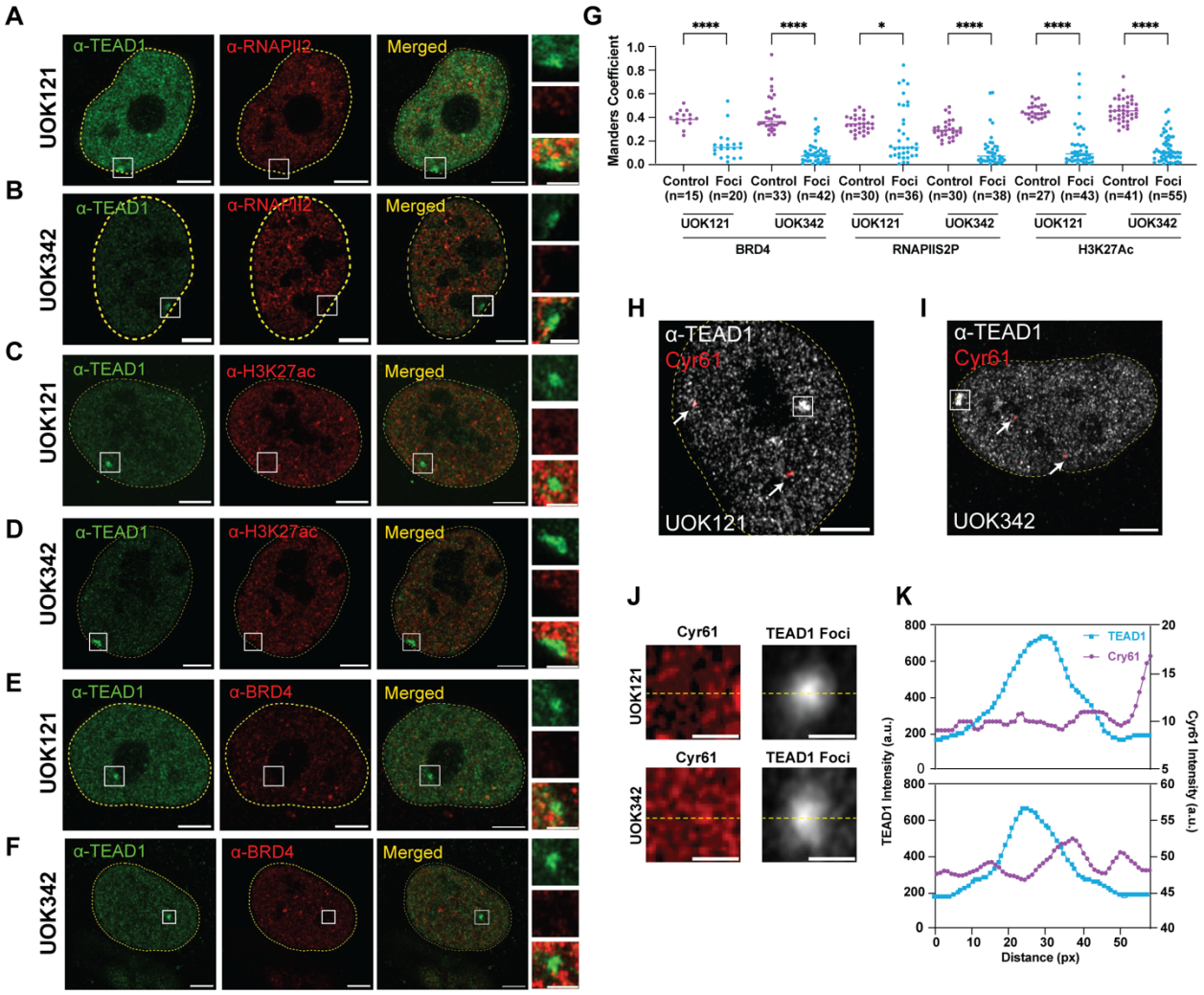


**Figure 2. TEAD1 foci are transcriptionally inactive.**

**(A–F)** Representative immunofluorescence images of TEAD foci (green) and active transcription markers (red): RNAPII2 in UOK121 **(A)** and UOK342 **(B)**, H3K27ac in UOK121 **(C)** and UOK342 **(D)**, and UOK121 **(E)** and UOK342 **(F)**. Insets show magnified boxed regions of merged channels with adjusted intensity. Scale bars = 2 µm. Nuclear boundaries indicated by dashed lines.

**(G)** Quantitative assessment and statistical evaluation of co-localization of TEAD1 with active transcription markers around foci and control regions. Data are presented as mean ± SEM.

**(H-I)** Representative images of TEAD1 foci and Fluorescence in Situ Hybridization (FISH) of nascent Cyr61 mRNA in UOK121 **(H)** and UOK342 **(I)**. Arrows indicating Cyr61 nascent mRNA signals and TEAD1 foci are highlighted with 50x50 pixel squares. Nuclear boundaries are indicated by dotted lines.

**(J)** Average images centered on TEAD1 foci, showing a lack of active transcription with decreased average Cyr61 intensity (red) in UOK121 (top, n=35) and UOK342 (bottom, n=20). Scale bars are 1μm.

**(K)** Line plots of TEAD1 foci and Cyr61 average intensity along the dashed line shown in **(J)** for UOK121 (top) and UOK342 (bottom). Blue line: TEAD1 intensity; magenta line: Cyr61 intensity.

Statistical significance determined by one-way ANOVA: ns, $p > 0.05$; *, $p \leq 0.05$; ****, $p \leq 0.0001$.

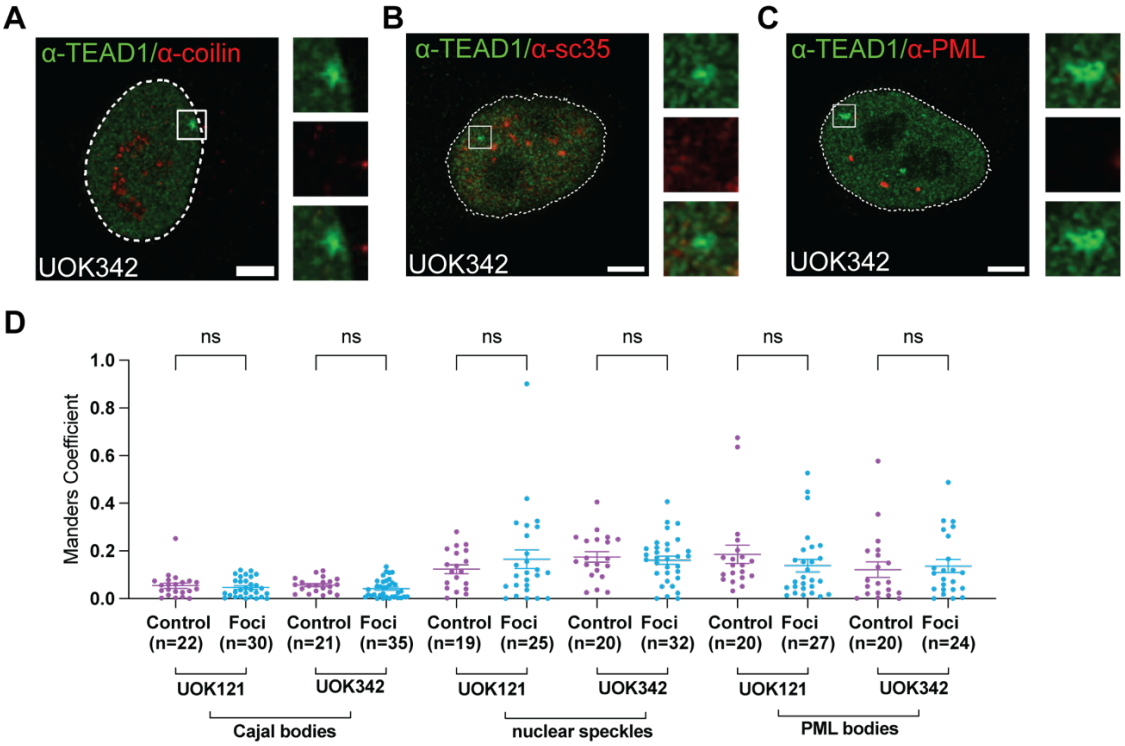


**Supplemental Fig. 2. TEAD1 foci do not colocalize with other nuclear bodies.**

**(A-C)** Representative UOK342 immunofluorescence images of TEAD1 foci (green) with various Nuclear Bodies (red): Cajal bodies **(A),** nuclear speckles **(B),** and PML bodies **(C)**. Scale bars are 5μm. Nuclear boundaries are indicated by dotted lines.

**(D)** Quantification of co-localization of immunofluorescence imaging of TEAD1 with indicated MLO markers in indicated cell lines around foci regions (foci) and randomly selected nuclear regions (control) in **(A-C)**. Data are presented as mean ± SEM.

Statistical significance determined by one-way ANOVA: ns, $p > 0.05$; *, $p \leq 0.05$; ****, $p \leq 0.0001$.

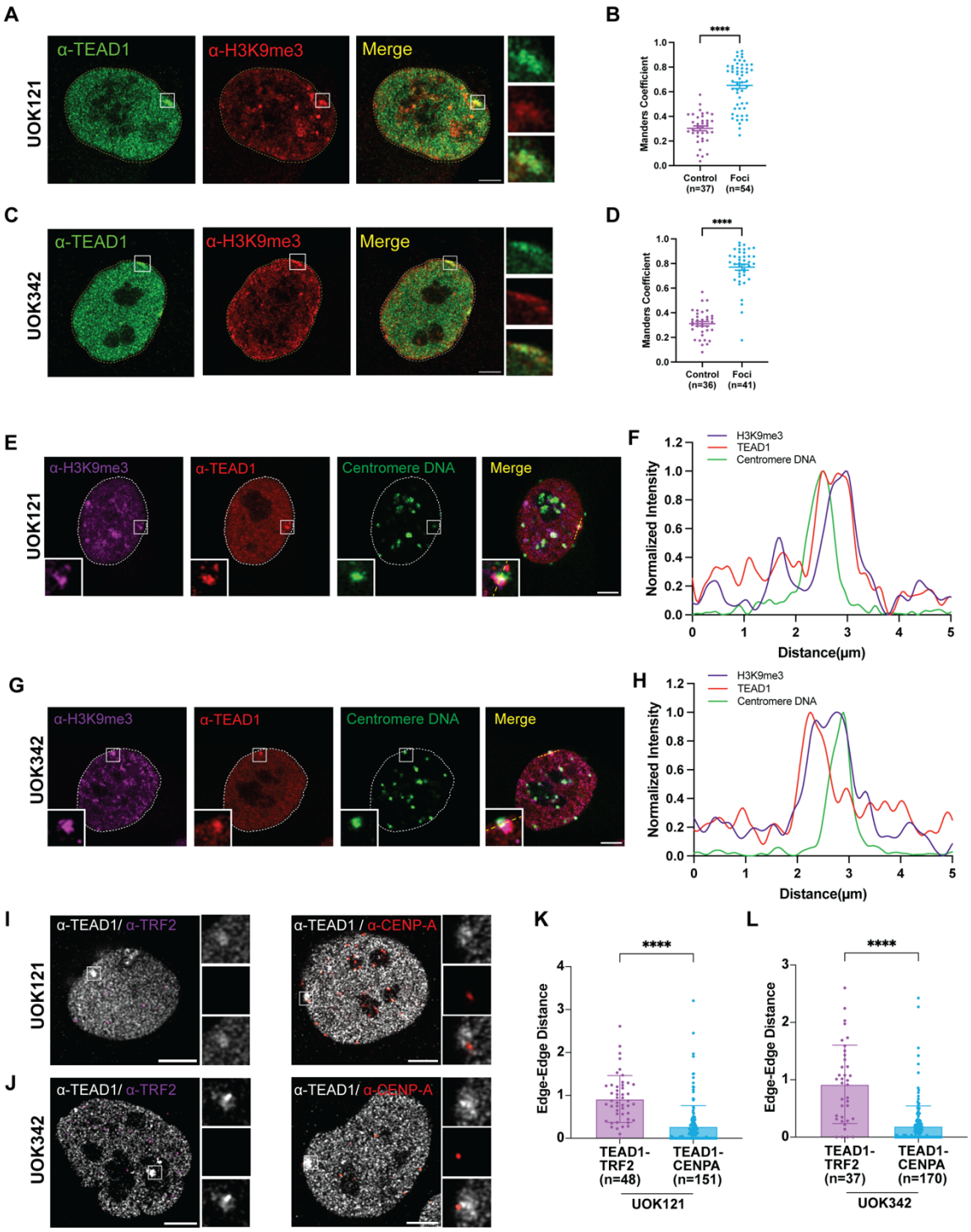


**Figure 3. Co-localization of TEAD1 foci with heterochromatin markers in different RCC cell lines**

**(A-D)** Representative immunofluorescence images of TEAD1 (green) and H3K9me3 (red) in UOK121 **(A)** and UOK342 **(C)** cells (scale bars are 5μm). Insets show magnified images of boxed

regions. Co-localization of TEAD1 foci and H3K9me3 in UOK121**(B)** and UOK342**(D)** compared to the more diffused TEAD1 region. Data are presented as scatterplots with mean ± SEM.

**(E-H)** Representative immunofluorescence images illustrate the co-localization of TEAD1 (red) with H3K9me3 (magenta) and adjacent to centromere DNA-FISH (green) and in UOK121 **(E)** and UOK342 **(G)** cells. Insets show magnified images of boxed regions. Scale bars are 5μm. Signal intensity profiles along the lines indicated on the merged-channel images for UOK121 **(F)** and UOK342 **(H)**.

**(I-L)** Representative immunofluorescence images and quantification illustrate the co-localization of TEAD1 (green) with TRF2 (magenta) and CENP-A markers (red) in UOK121 **(I)** and UOK342 **(J)**. Insets show magnified images of boxed regions. Quantification uses 3D nearest neighbor analysis in UOK121 **(K)** and UOK342 **(L)**, demonstrating a tighter distribution of CENP-A at a smaller minimal distance. Data are presented as mean ± SD.

Statistical significance determined by unpaired t-test: ns, $p > 0.05$; *, $p \leq 0.05$; ****, $p \leq 0.0001$.

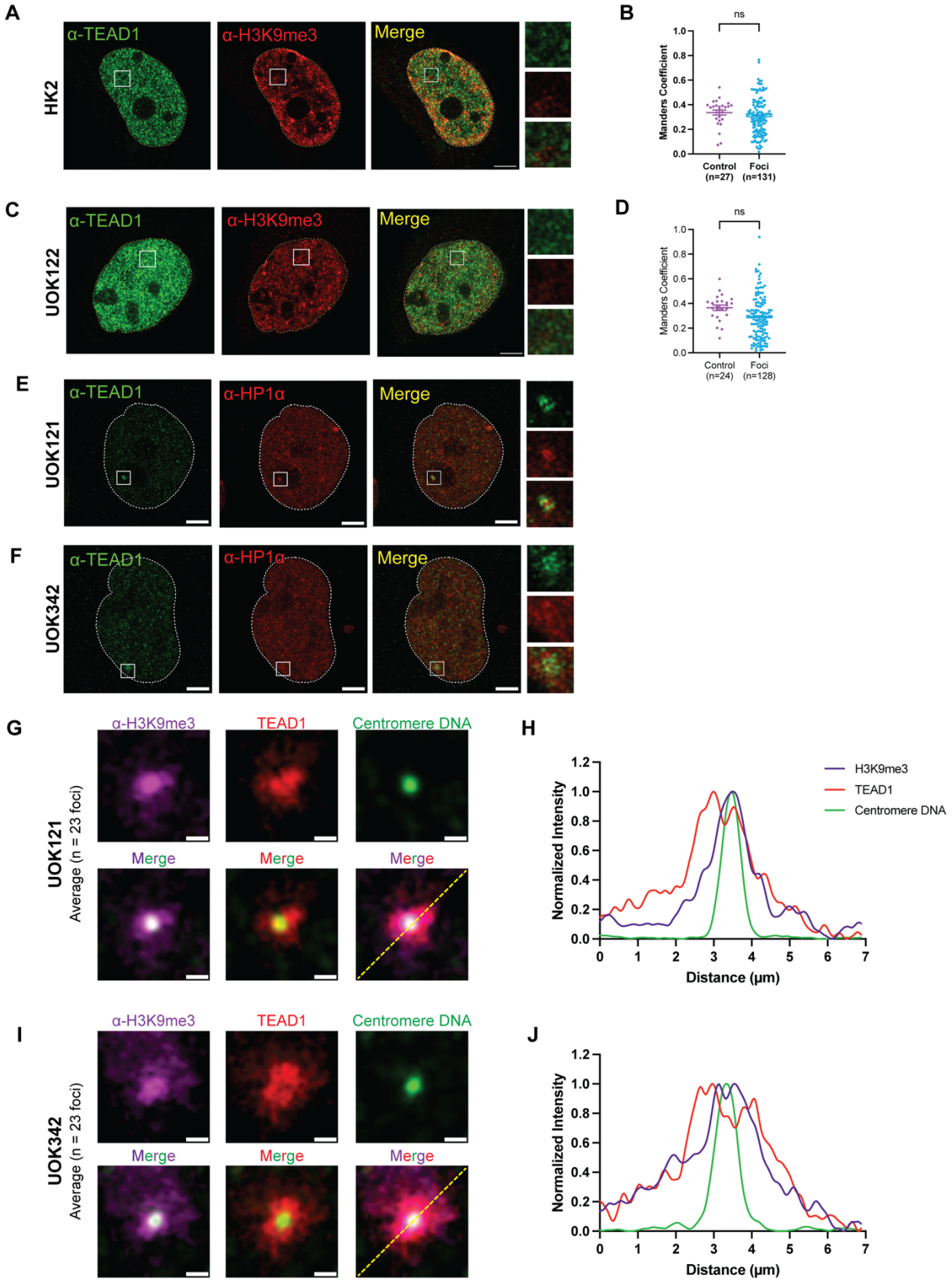


**Supplemental Fig. 3. Co-localization of TEAD1 foci with heterochromatin markers.**

**(A-D)** Representative immunofluorescence images of TEAD1 (green) and H3K9me3 (red) in HK2 **(A)** and UOK122 **(B)** cells (scale bars are 5 μm). Insets show magnified images of boxed regions. Co-localization analysis between TEAD1 and H3K9me3 around TEAD1 foci (foci) and control nuclear regions (control) in HK2 **(C)** and UOK122 **(D)** cells. Data are presented as scatterplots with medians.

**(E-F)** Representative immunofluorescence images illustrate the co-localization of TEAD1 (green) with HP1 (red) in UOK121 **(E)** and UOK342 **(F)** cells. Insets show magnified images of boxed regions.

**(G-J)** Average intensities of images centered at the centromere in UOK121 **(G)** and UOK342 **(I)**. UOK121 n=23 foci, UOK342 n=23 foci. Line plots of H3K9me3 (magenta line), TEAD1 (red line), and centromere DNA-FISH signal (green line) in UOK121 **(H)** and UOK342 **(J)**.

Statistical significance determined by unpaired t-test: ns, $p > 0.05$; *, $p \leq 0.05$; ****, $p \leq 0.0001$.

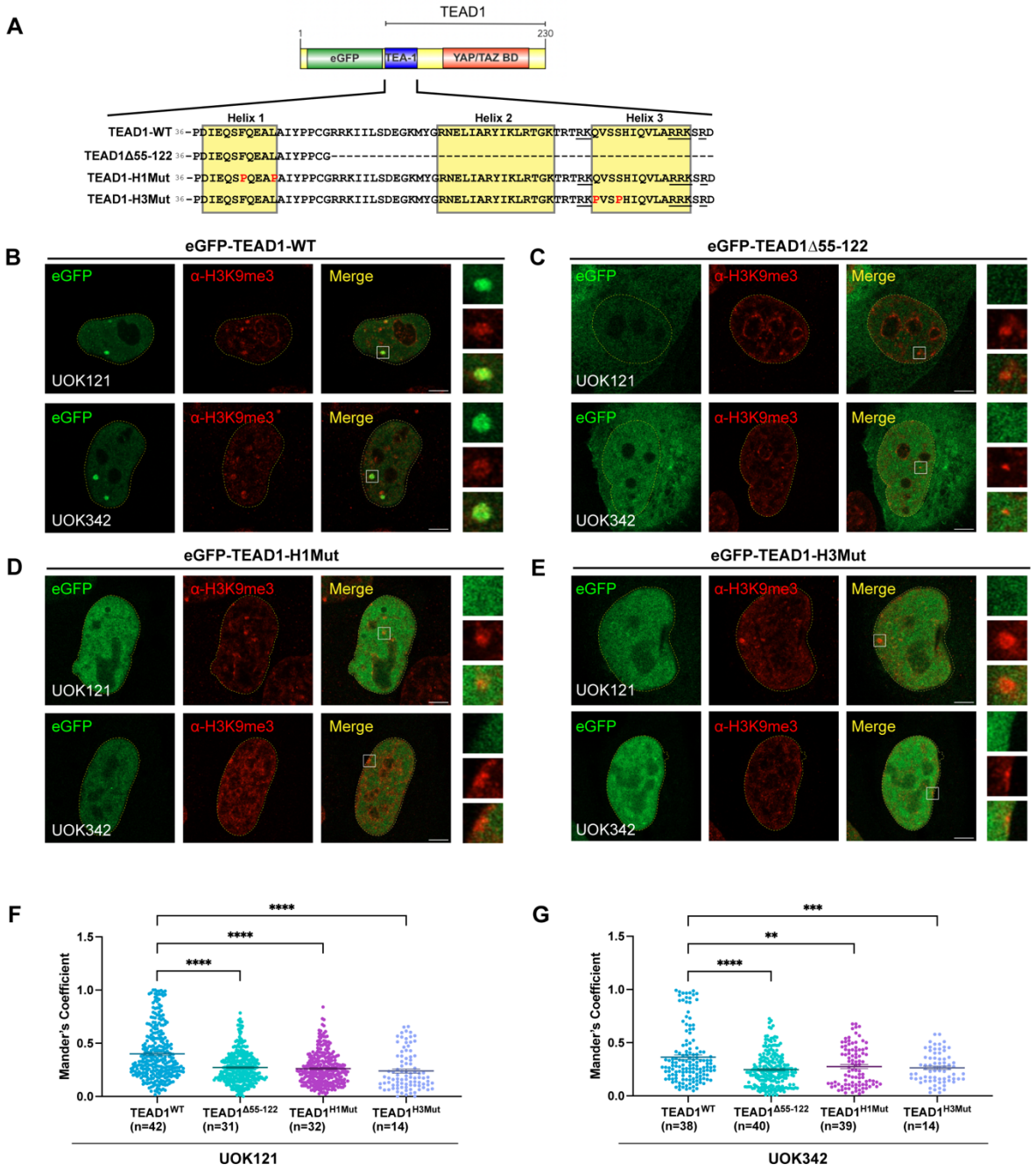


**Figure 4. TEAD1 foci formation is dependent on DNA-binding ability.**

**(A)** Schematics of eGFP-TEAD1 constructs with wild-type TEAD1, TEAD1 DNA-binding domain (DBD) deletion, TEAD1 helix 1 (H1) mutant, and TEAD1 DBD helix 3 (H3) mutants. The underlined amino acid sequence represented the TEAD1 nuclear localization signal (NLS), and the red amino acids are mutated in the respective mutants.

**(B-E)** Representative images of UOK121 and UOK342 cells expressing eGFP-TEAD1-WT **(B)**, eGFP-TEAD1-DBD deletion (**C**), eGFP-TEAD1-H1mut (**D**), and eGFP-TEAD1-H3mut (**E**), with

immunofluorescence signal of H3K9me3 (red). Insets show magnified images of boxed regions. Scale bars are 5µm.

**(F-G)** Quantification of co-localization between H3K9me3 and eGFP-TEAD1 variants signals shown in (B-E). Data are presented as scatterplots with means ± SEMs.

Statistical significance determined by one-way ANOVA comparing different mutants to the $TEAD1^{WT}$: ns, $p > 0.05$; **, $p \leq 0.002$; ***, $p \leq 0.0002$; ****, $p \leq 0.0001$,

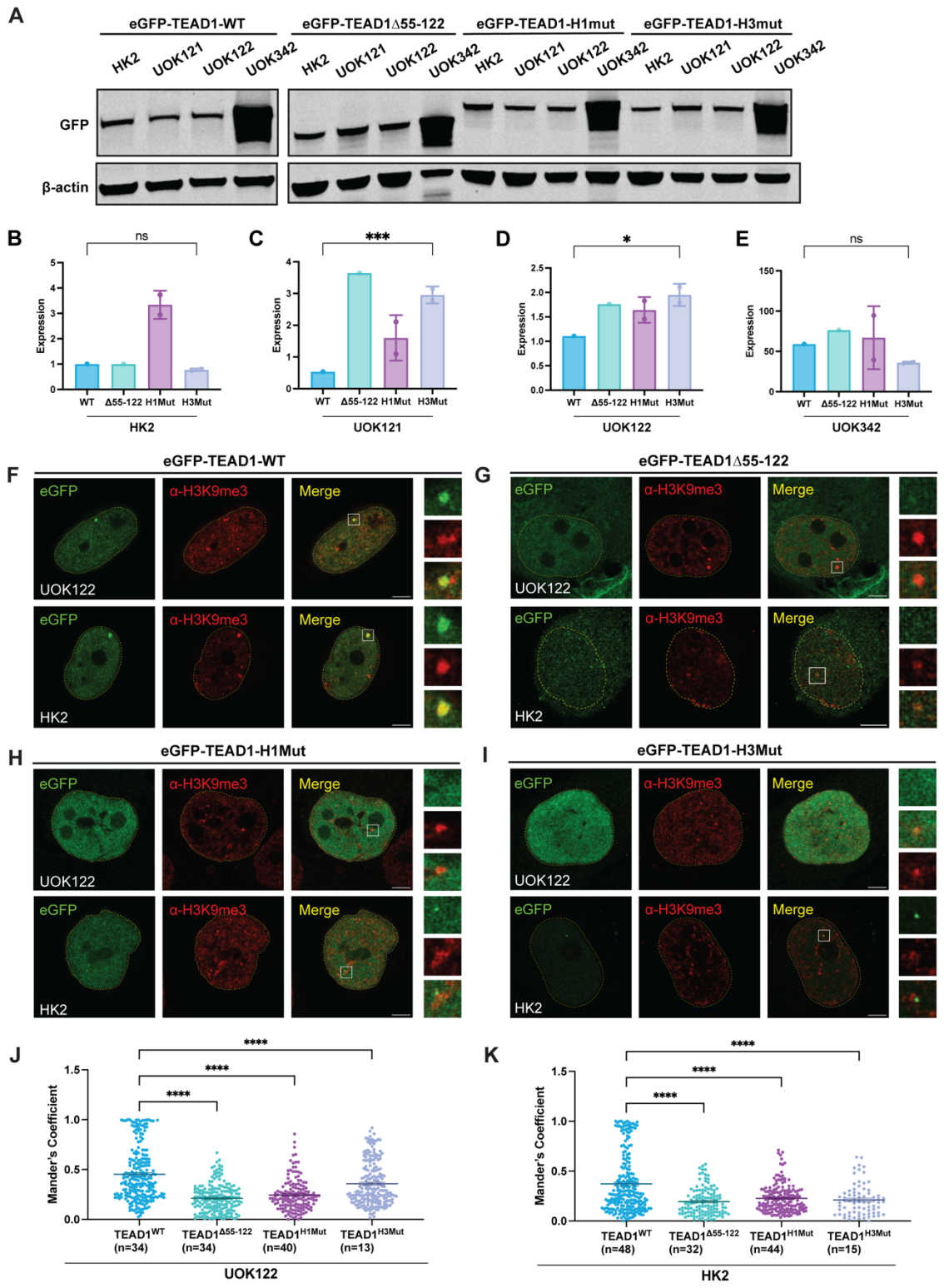


**Supplemental Fig. 4. TEAD1 foci formation is dependent on DNA-binding ability.**

**(A)** Immunoblot shows eGFP expression level after transfection in HK2 and UOK cell lines.

**(B-E)** Quantification of immunoblot proteins expression levels in **(A)** with GFP antibodies across different indicated cell lines. Statistics: unpaired t test comparing eGFP-TEAD1-WT and eGFP-TEAD1-H3mut expression levels.

**(F-I)** Representative images of UOK122 and HK2 cells expressing eGFP-TEAD1-WT (F), eGFP-TEAD1-DBD deletion (**G**), eGFP- TEAD1-H1mut (**H**), and eGFP- TEAD1-H3mut (**I**), with immunofluorescence signal of H3K9me3 (red). Insets show magnified images of boxed regions. Scale bars are 5μm.

**(J-K)** Quantification of co-localization between H3K9me3 and eGFP signal shown **(F-I)** in UOK122 (**J**) and HK2 (**K**) cells. Data are presented as scatterplot with mean ± SEM. Statistical significance determined by one-way ANOVA: ns, $p > 0.05$; *, $p \leq 0.05$; ****, $p \leq 0.0005$.

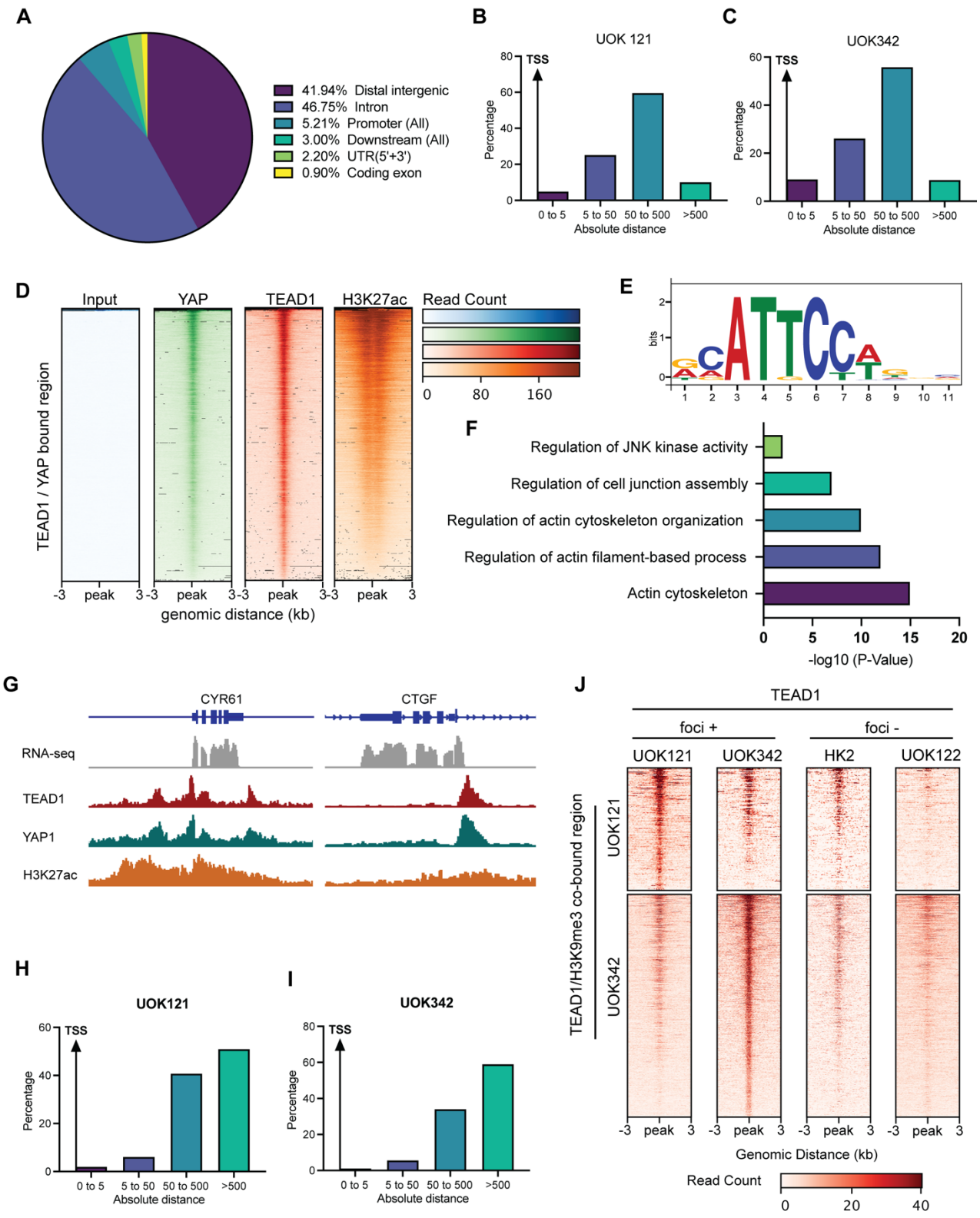


**Figure 5. TEAD1 binds to both enhancers and heterochromatin regions in the genome.**

**(A)** TEAD1 peaks were mapped back to various regions of the genome. The percentage of the TEAD1 peaks found within each region of the genome is shown in the pie chart.

**(B-C)** Bar graph from GREAT analysis showing the percent distribution of TEAD1 peaks in relation to the transcription start site (TSS) of genes in UOK121 (**B**) and UOK342 (**C**) cells. Distance to TSS is shown in kilobases (kb).

**(D)** Heatmaps showing merged TEAD1, and H3K27ac ChIP-seq signals (merged data from HK2, UOK121, UOK122, UOK342). Active enhancer regions are shown as regions that have H3K27ac peaks.

**(E)** Motif analysis of TEAD1-bound peaks showing the most significant M-CAT motif in 348 sites.

**(F)** Gene ontology analysis of TEAD1-bound peaks using DAVID.

**(G)** Gene tracks showing TEAD1 and YAP1 co-binding at the H3K27ac region of CTGF (left) and Cyr61 (right) genes, with their corresponding mRNA expression profiles.

**(H-I)** Bar graphs from GREAT analysis showing the percent distribution of TEAD1-H3K9me3 co-peaks in relation to the transcription start site (TSS) of genes in UOK121 **(H)** and UOK342 **(I)**. Distance to TSS is shown in kilobases (kb).

**(J)** Heatmaps showing TEAD1 ChIP signals across cell lines at TEAD1/H3K9me3 co-binding regions of UOK121 (top) and UOK342 (bottom).

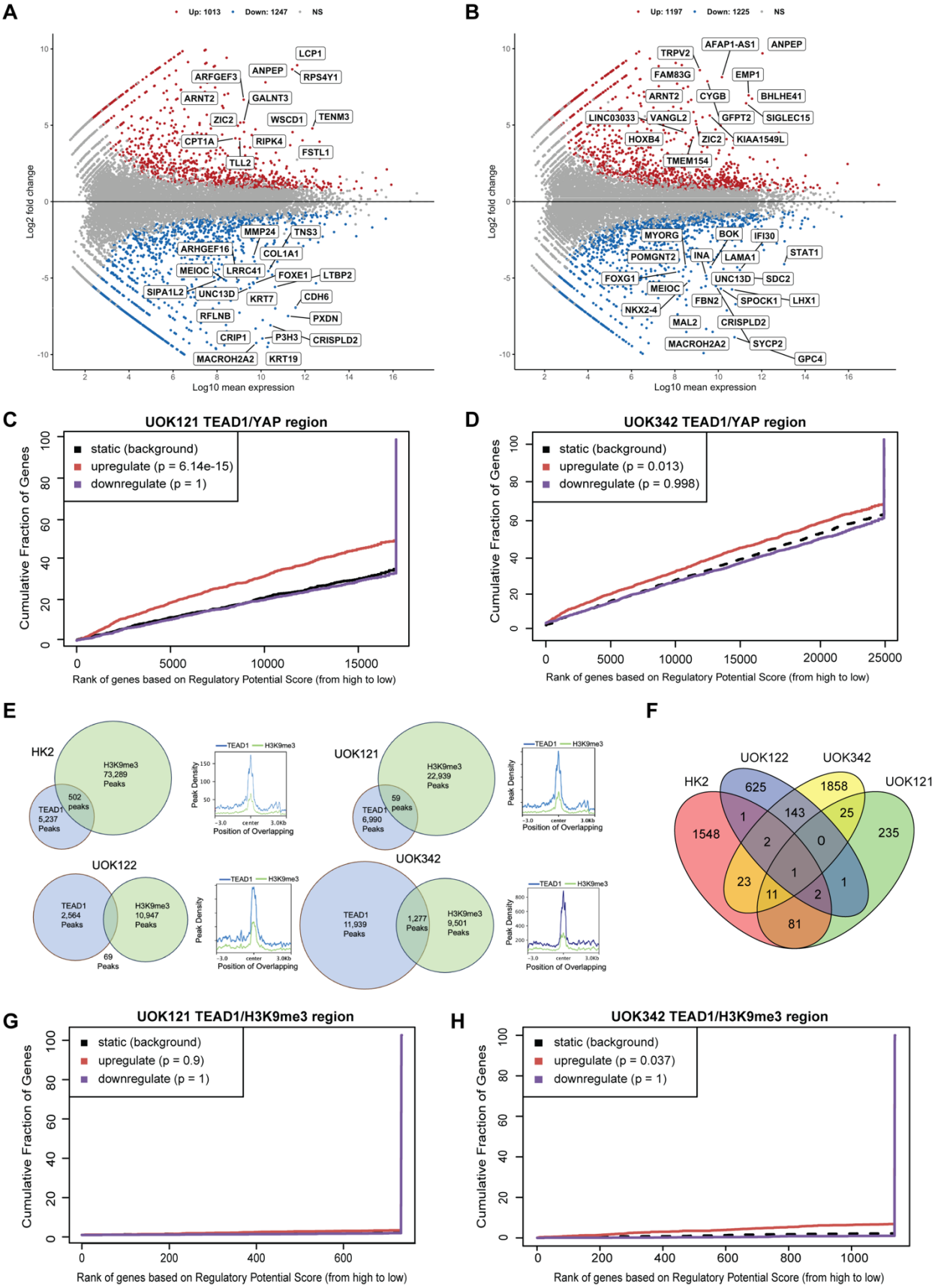
A
Up: 1013
Down: 1247
NS
LCP1
ANPEP
RPS4Y1
ARFGEF3
ARNT2
GALNT3
ZIC2
WSCD1
TENM3
CPT1A
RIPK4
FSTL1
TLL2
MMP24
TNS3
ARHGEF16
COL1A1
MEIOC
LRRC41
FOXE1
LTBP2
SIPA1L2
UNC13D
KRT7
CDH6
RFLNB
PXDN
CRIP1
P3H3
CRISPLD2
MACROH2A2
KRT19
Log2 fold change
Log10 mean expression
B
Up: 1197
Down: 1225
NS
TRPV2
AFAP1-AS1
ANPEP
FAM83G
EMP1
ARNT2
CYGB
BHLHE41
LINC03033
VANGL2
GFPT2
SIGLEC15
HOXB4
ZIC2
KIAA1549L
TMEM154
MYORG
BOK
IFI30
POMGNT2
INA
LAMA1
STAT1
FOXG1
MEIOC
UNC13D
SDC2
FBN2
SPOCK1
LHX1
NKX2-4
MAL2
CRISPLD2
MACROH2A2
SYCP2
GPC4
Log2 fold change
Log10 mean expression
C
UOK121 TEAD1/YAP region
static (background)
upregulate (p = 6.14e-15)
downregulate (p = 1)
Cumulative Fraction of Genes
Rank of genes based on Regulatory Potential Score (from high to low)
D
UOK342 TEAD1/YAP region
static (background)
upregulate (p = 0.013)
downregulate (p = 0.998)
Cumulative Fraction of Genes
Rank of genes based on Regulatory Potential Score (from high to low)
E
HK2
H3K9me3
73,289
Peaks
502
peaks
TEAD1
5,237
Peaks
UOK121
H3K9me3
22,939
Peaks
59
peaks
TEAD1
6,990
Peaks
UOK122
TEAD1
2,564
Peaks
H3K9me3
10,947
Peaks
69
Peaks
UOK342
TEAD1
11,939
Peaks
1,277
Peaks
H3K9me3
9,501
Peaks
TEAD1
H3K9me3
Peak Density
Position of Overlapping
F
HK2
UOK122
UOK342
UOK121
625
1858
1548
1
143
25
235
2
0
23
1
11
2
1
81
G
UOK121 TEAD1/H3K9me3 region
static (background)
upregulate (p = 0.9)
downregulate (p = 1)
Cumulative Fraction of Genes
Rank of genes based on Regulatory Potential Score (from high to low)
H
UOK342 TEAD1/H3K9me3 region
static (background)
upregulate (p = 0.037)
downregulate (p = 1)
Cumulative Fraction of Genes
Rank of genes based on Regulatory Potential Score (from high to low)

**Supplemental Fig. 5. ChIP-seq reveals universal binding sites of TEAD1 foci.**

**(A-B)** MA plots showing differential gene expression from RNA-seq analysis comparing UOK121 **(A)** and UOK342 **(B)** to HK2 cells. Gene expression is plotted as $\log_2$ fold change (y-axis) versus $\log_{10}$ mean expression (x-axis). Red dots represent significantly upregulated genes and blue represent downregulated genes ($p \leq 0.01$). Non-significant genes are shown in gray.

**(C-D)** Line graph showing correlation of TEAD1 ChIP-seq binding data with differential gene expression in UOK121 **(C)** and UOK342 **(D)** using Binding and Expression Target Analysis (BETA). Genes were ranked by regulatory potential score (x-axis) based on ChIP-seq peaks that are co-bound by TEAD1 and YAP. Cumulative fractions of upregulated (red), downregulated (purple), and static (black) genes were plotted (y-axis).

**(E)** Venn diagram representing uniquely mapped TEAD1 peaks in HK2 and UOK cell lines, overlapped regions of H3K9me3, followed by line plot distribution of TEAD1 and H3K9me3 enrichment centered around overlapped regions. Distance to TEAD1 peaks is shown in kb.

**(F)** Venn diagram representing shared TEAD1 overlapped regions of H3K9me3 across cell lines.

**(G-H)** Line graph showing correlation of TEAD1 ChIP-seq binding data with differential gene expression in UOK121 **(G)** and UOK342 **(H)** using BETA. Genes were ranked by regulatory potential score (x-axis) based on ChIP-seq peaks that are co-bound by TEAD1 and H3K9me3. Cumulative fractions of upregulated (red), downregulated (purple), and static (black) genes were plotted (y-axis).

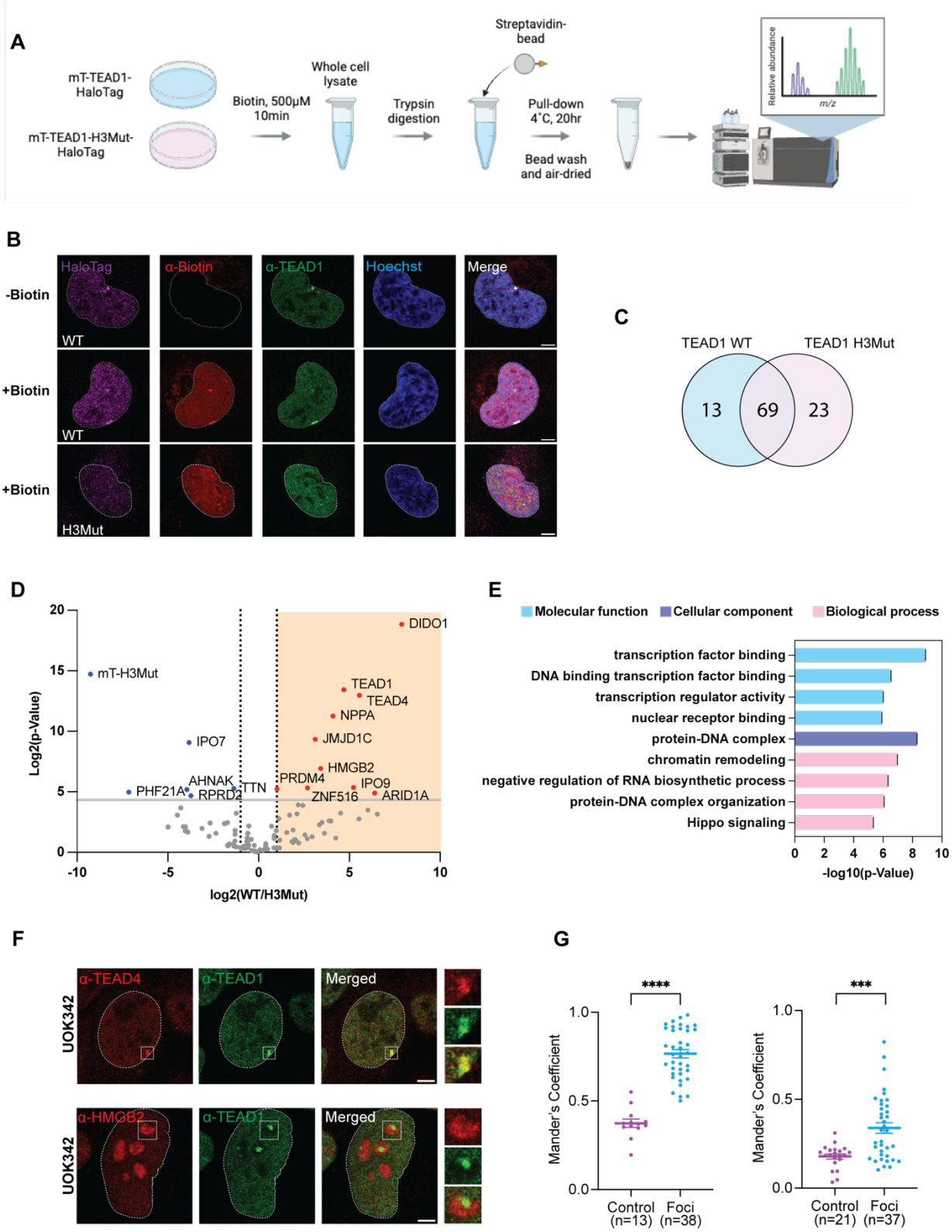


**Figure 6. Identification of protein components of TEAD1 foci with proximity-based mass spectrometry.**

**(A)** Schematic of the proximity labeling experimental setup for protein identification in TEAD1 foci. mT is short for miniTurbo.

**(B)** Representative immunofluorescence images of UOK342 transiently expressing miniTurbo-TEAD1 WT-HaloTag (WT) and miniTurbo-TEAD1 H3 mutant-HaloTag (H3Mut) showing biotinylation (red) in relation to HaloTag (magenta), TEAD1 (green), and nuclei (blue). Scale bars represent 5 μm.

**(C)** Venn diagram summarizing unique and shared biotin-peptides identified in mass spec between TEAD1 WT and TEAD1 H3Mut.

**(D)** Volcano plots showing differentially enriched biotinylated proteins comparing WT / H3Mut (n=3 WT and n=3 H3Mut). Red symbols (two-sided t test unadjusted $p \leq 0.05$ and ≥ 2-fold change) represent biotinylated proteins enriched in cells expressing miniTurbo-TEAD1 WT-HaloTag, and blue symbols represent biotinylated proteins enriched in cells expressing miniTurbo-TEAD1 H3Mut-HaloTag.

**(E)** Results from GSEA of ≥ 2-fold biotinylated proteins in miniTurbo-TEAD1 WT-HaloTag showed enrichment of chromatin remodeling and negative regulation on transcription.

**(F)** Representative images of TEAD4 colocalizing with TEAD1 foci and HMGB2 colocalizing with the nucleolar-localized TEAD1 foci. Scale bars represent 5 μm.

**(G)** Quantification of co-localization of TEAD1 with TEAD4 (left) and HMGB2 (right) in UOK342 cells around TEAD1 foci (foci) versus another random nuclear region (control). Mean ± SEM, ***, $p \leq 0.0005$; ****, $p \leq 0.0001$. Unpaired t-test.

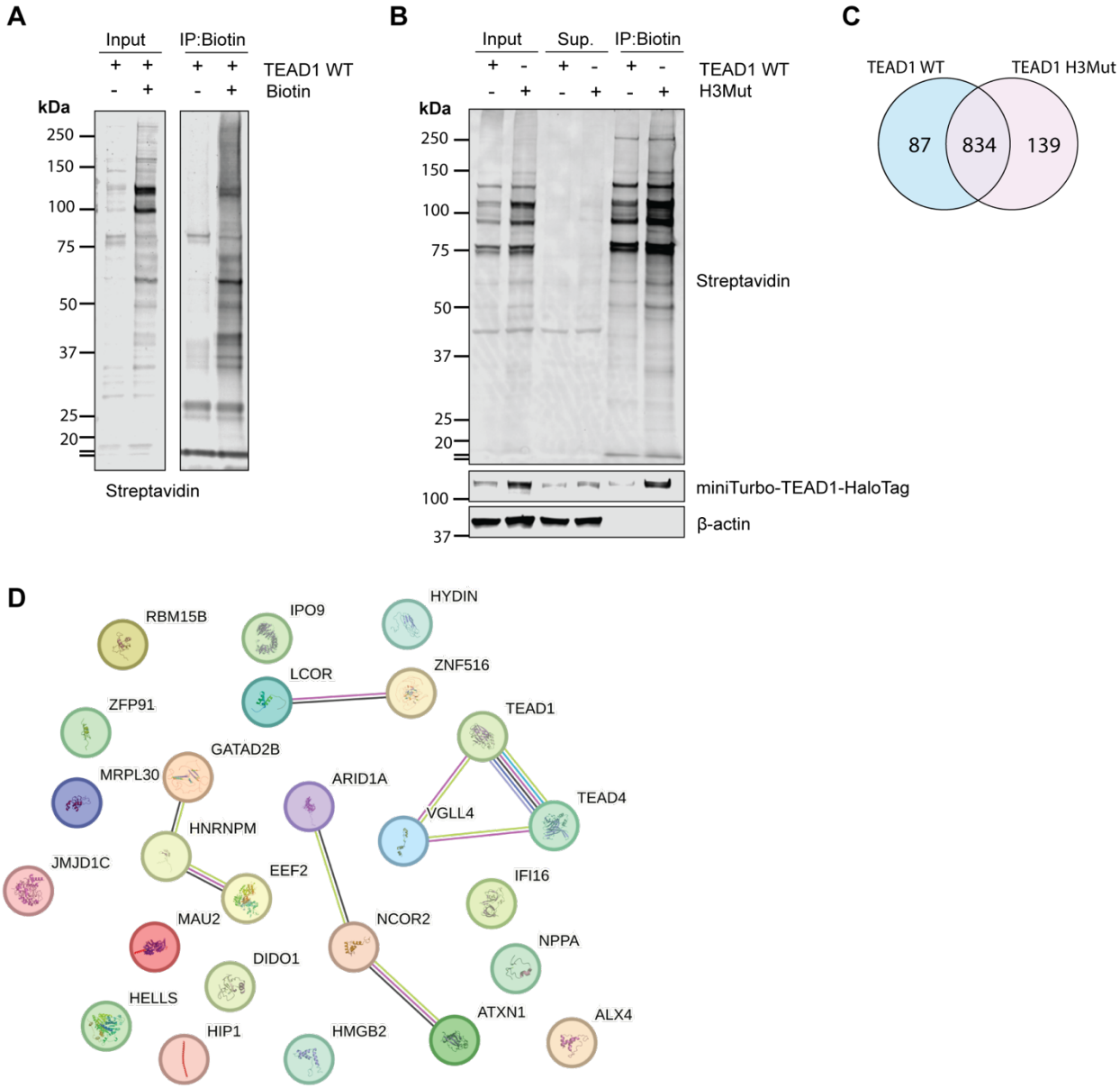


**Supplemental Figure 6. Identification of protein components of TEAD1 foci with proximity-based mass spectrometry.**

**(A)** Western blot showing enriched biotinylated proteins (Streptavidin IRDye680) with or without biotin treatment of UOK342 cells expressing miniTurbo-TEAD1-HaloTag.

**(B)** Western blot comparing biotinylated protein enrichments of miniTurbo-TEAD1 WT-HaloTag and miniTurbo-TEAD1 H3Mut-HaloTag expressed in UOK342 cells upon biotin treatment.

**(C)** Venn diagram summarizing all unique and shared proteins between TEAD1 WT and TEAD1 H3Mut identified in the mass spec.

**(D)** STRING analysis revealed protein-protein interaction networks of candidate TEAD1 foci components, corresponding to the GO enrichment analysis shown in Fig. 6E.

## Method

### Cell culture, transfection, and siRNA

Patient-derived immortalized cell lines UOK121, UOK139, UOK140, and UOK275 cells were gifted from Dr. Marshall Linehan's Lab. HK-2 is from ATCC (CRL-2190). Cells are cultured at 37°C and 5% CO2 in DMEM supplemented with 10% fetal bovine serum (FBS; Gibco, 26140079), 100 U/mL (1%) penicillin/streptomycin (Gibco, 15140122), 2 mM (1%) GlutaMAX-I (Gibco,35050061), 1x NEAA (Gibco, 11140050). For overexpression experiments UOK and HK2 cells were transfected with eGFP-TEAD1, eGFP-TEAD1-Δ55-122, eGFP-TEAD1-H1mut, eGFP-TEAD1-H3mut, using Lipofectamine 3000 Transfection Reagent (cat. no. L3000015), for 16 h. For siTEAD1 experiments, TEAD1 siRNA (Thermo Fisher, Silencer Select s13962) or scrambled negative control siRNA was used at a final concentration of 10 nM (Thermo Fisher, AM4611), and was transfected into cells using the Lipofectamine RNAiMAX transfection reagent (Thermo Fisher, cat. no. 13778075) for 48 h, after which cells were replated for Western blot and imaging.

### Cell lines generation

**UOK342 HaloTag-TEAD1 KI cell line generation.** Endogenously tagged UOK342 Halo-Tag KI cells were engineered using CRISPR-Cas9 system. pTEAD1-gDNA targeting the N-terminus of TEAD1 was assembled into PX458 template plasmid (Addgene #48138) using the forward primer CACCGAAAGGCTCCAGGCTTCGGCT and the reverse primer aaacAGCCGAAGCCTGGAGCCTTTC. pTEAD1-donor was assembled into pUC57mini (Addgene #88845) using gblock containing HaloTag sequence and 300bp homology arms of the gDNA target site. UOK342 cells were transfected with lipofectamine 3000 (L3000015, ThermoFisher) following the manufacture's protocol. The cells were cultured for >14 days and sorted into single colonies by fluorescence-activated cell sorting (FACS) and expanded. The genomic DNA from the selected clone was extracted using GeneJET Genomic DNA Purification Kit (K0721, Thermo Scientific) and performed PCR using the forward primer

TTCTGCCCACCATTGCATTTCTGTG and the reverse primer GTATGGTAAGTGGCCTGGAACACTCC with Q5 High-Fidelity 2X
901 Master Mix (M0492, NEB). The PCR product was gel extracted using Monarch DNA Gel
902 Extraction Kit (T1020S, NEB) and verified using Sanger sequencing.

**miniTurbo plasmid construct and stable cell line generation.** miniTurbo-TEAD1-HaloTag and miniturbo-TEAD1 H3Mut-HaloTag expression plasmids were made with the eGFP-TEAD1 vector and the following primers for cloning: miniTurbo N-terminus f: ttagtgaaccgtcagatccgctagcgccaccatgatcccgctgctgaacgct; TEAD1 N-terminus f: ggcgctcctggctccgccggatctgcagctggtggatccggaattgagcccagcagctgg; HaloTag C-terminus r: atctagatccggtggatctgaattctcatcagccggaaatctcgagcgtc. Plasmids were validated by whole-plasmid sequencing (Plasmidsaurus). For cell line generation, miniturbo-TEAD1-HaloTag and miniturbo-TEAD1 H3Mut-HaloTag plasmids were transfected in UOK342 cells using Lipofectamine 3000 Transfection Reagent (L3000015, ThermoFisher) and passaged for >14 days. Cells were stained for 30 min with JFX549-HaloTag ligand (100nM, Janelia Materials). Cellswith stable expression were sorted by fluorescence-activated cell sorting (FACS) and expanded. Expression of the fusion proteins were validated using western blot.

**Immunofluorescence staining**

After transfection, UOK and HK2 cells were plated on coverslips pre-coated with fibronectin (7.5 µg/mL; Millipore, FC010). Cells were grown for 16 hours and fixed with 4% FA (EMS), permeabilized with 0.1% Triton X-100, and blocked with 3% BSA in 1X PBS. The cells were then incubated overnight with primary antibodies in 1% BSA at 4°C, and then incubated with Alexa Fluor-conjugated secondary antibodies in 1% BSA for 1 h at RT. The following primary and secondary antibodies were used: anti-YAP (1:150; Cell Signaling, 14074S); anti-TEAD1 (BD Biosciences; 610923); anti-BRD4 (Abcam; 207057); anti-TEAD2 (Abcam; 54374), anti-TEAD3

(Abnova; H00007005-MO1), anti-TEAD4 (Abcam; 58310), anti-H3K27ac (Active Motif; 39685), anti-H3K9me3 (Active Motif; 39161), anti-RNAPIIS2P (Abcam; 193468), anti-coilin (Abcam; 87913), anti-PML (Abcam; 96051), anti- sc35 (Abcam; 11826), AmyTracker680 (Ebba Biotech), anti-nucleolin (14574, Cell Signaling), Goat anti-Rabbit IgG (H+L) Cross-Adsorbed Secondary Antibody, Alexa Fluor 568 (1:1000; Thermo fisher, A11011). Nuclei were labeled with 1:5000 Hoechst 33342 (Thermo Fisher, cat. no. 62249). For imaging and quantification, at least 20 fields of view per coverslip were randomly chosen by Hoechst nuclear staining and imaged using a Zeiss LSM900 Airyscan microscope, followed by Airyscan processing (2D, default settings).

**Domain deletion and site-directed mutagenesis**

The plasmid eGFP-TEAD1 was first digested using BamHI and ApaI to create the backbone. This step was followed by the amplification of two specific DNA fragments using polymerase chain reaction (PCR). The primer sets used for the first fragment were TEAD1-1f (5' tggccgccatCCCACATGGTGGATAGATAG 3') and TEAD1-1r (5'-tcaagcttcgaattgtacagGATCCATTGAGCCCAGCAG 3'), and for the second fragment were TEAD1-2f (5'-accatgtgggATGGCGGCCATGTCCTCA 3') and TEAD1-2r (5' aagaaggcattttgagggcccTTTCCAAACAGTTCCTTTAAGCCAC 3'). These PCR products were then ligated into the prepared backbone using high-fidelity HIFI assembly. To construct the eGFP-TEAD1-H3mut variant, the process began with BamHI digestion of eGFP-TEAD1, followed by PCR to generate two segments. These segments were amplified using primer pairs TEAD1-3f (5’-TCAAGCTTCGAATTGTACAGG-3’) and TEAD1-3r (5’-AGGAGACACCGGTTTTCTGGTCCTCGTC-3’), and TEAD1-4f (5’-CCAGAAAACCGGTGTCTCCTCACATTCAGGTTCTTGCC-3’) and TEAD1-4r (5’-CAAAAGGCTTGACGTCTTGTG-3’) respectively. These fragments were then assembled with the digested backbone using HIFI assembly. For the creation of eGFP-TEAD1-H1mut, PCR amplification was performed to produce three distinct fragments. The first fragment utilized

primers TEAD1-3f and TEAD1-5r (5'-ATAGCCgGGGCCTCCTGAggGCTTTGCTCGATGTCGGG-3'), the second employed TEAD1-5f (5'-ccTCAGGAGGCCCcGGCTATCTATCCACCATGTG-3') and TEAD1-4r, and the third fragment was a previously prepared backbone. These PCR fragments were subsequently assembled into the final construct through the HIFI assembly method.

**DNA Fluorescence *in-situ* hybridization (FISH) and immunofluorescence staining of TEAD1 foci**

UOK and HK2 cells were plated on #1.5H high-performance coverslips (Marienfeld Superior) pre-coated with fibronectin (7.5 µg/mL; Millipore, FC010). Cells were grown overnight, washed with 1X PBS and fixed with 4% methanol-free formaldehyde (Cell Signaling 12606) /1X PBS) for 10 minutes. Coverslips were washed in 1X PBS / 0.002% Tween (PBS-T) 5 times with a transfer method detailed in [74], and permeabilized with 0.2% Triton-X-100 for 10 minutes before blocking in MaxBlock (Active Motif 15252) for 1 hour. Coverslips were incubated overnight in primary antibody (H3K9me3, Active Motif 39161 1:500; TEAD1, BD 610922 1:200) in MaxBlock, and washed 5X in PBS-T. Secondary antibodies (AF647 1:500; AF594 1:1000) were incubated in MaxBlock for 1 hour in the dark, and washed 5X in PBS-T before post-fixation in 4% methanol-free formaldehyde for 10 minutes. Subsequently, FISH hybridization for centromere probes was performed as described[75]. AF488-labelled probes (gift from Alan Meeker) suspended in hybridization buffer were denatured at 84°C for 5 minutes before hybridization at room temperature for 2 hours. Coverslips were then washed 2X in PNA buffer for 15 minutes at room temperature, then washed 2X in PBS-T and counterstained with Hoescht 33342 at 1:5000, before washing 2X in PBS-T, once in ddH2O, pre-equilibrating and mounting in Vectashield before proceeding to Airyscan imaging.

**Intron RNA FISH combined with immunofluorescence**

Human *Cyr61*_intron with Quasar 570 dye (Biosearch Technologies, ISMF-2066-5), human *ACTB*_intron with Quasar 570 dye (Biosearch Technologies, ISMF-2002-5), Stellaris RNA FISH Hybridization Buffer (Biosearch Technologies, SMF-HB1-10), Stellaris RNA FISH Wash Buffer A (Biosearch Technologies, SMF-WA1-60) and Wash Buffer B (Biosearch Technologies, SMF-WB1-20) are purchased from Biosearch Technologies. We followed the protocol for sequential IF + FISH in Adherent Cells listed on the Biosearch Technologies website under Stellaris RNA FISH protocols.

**Image analyses**

**TEAD1 foci nuclear localization quantification.** Immunofluorescence staining against of UOK121 and UOK342 cell lines was performed. 3D images were acquired using Zeiss LSM 900 with Airyscan 2 detector. Z-stacks were captured at 0.15 μm intervals and 3D Airyscan processing was applied. TEAD1 foci localization was analyzed in 3D using Zeiss Zen software. Nucleoli were identified based on nucleolin staining, and perinuclear regions were defined as areas within 1 μm of the nuclear envelope, as delineated by Hoechst staining. TEAD1 foci were considered colocalized with the nucleolus if they overlapped with nucleolin-positive regions in 3D space. Similarly, TEAD1 foci were classified as perinuclear if they were located within 1 μm of the nuclear envelope. Colocalization was visually confirmed in all three dimensions. The percentage of TEAD1 foci localized to the nucleolus, perinuclear regions, both, or neither was calculated for each cell line. For representative images, maximum projections of the Z-stack were generated in Fiji.

**Co-localization analysis.** A square region measuring 3μm by 3μm was delineated around the focal point of TEAD1 foci. Additionally, a negative control square was randomly selected within the nucleoplasm where TEAD1 staining appeared diffused. The colocalization analysis was

conducted using FIJI software[76] with BIOP-JACoP plugin[77]. Statistical evaluation was performed using an unpaired T-test in GraphPad prism.

**3D Distance Analysis**. Immunofluorescence staining of HK2 and UOK cell lines was performed. The imaging was conducted using Airyscan Z-stacks with a z-interval of 0.13 μm. Three-dimensional distance analysis of TEAD1 foci with CENP-A or TRF2 was performed using ImageJ plugin Distance Analysis (DiAna)[78]. Specific thresholds were applied to different IF staining in the DiAna-segment module: a threshold of 5347 with a size larger than 1 pixel for CENPA, 2250 with a size larger than 1000 pixels for TEAD1 foci, and 8405 with a size larger than 30 pixels for TRF2. Using the DiAna-analysis module, the minimal distance of each TEAD1 foci to CENPA or TRF2 was determined. Distance histograms, visualizations, and statistical analyses were conducted using GraphPad Prism.

**Live cell imaging, Drug Treatment, Fluorescence recovery after photobleaching (FRAP)**

The TEAD1–HaloTag CRISPR knock-in UOK342 cells were plated into 64-well glass bottom plate (Cellvis, P96-1.5H-N) for drug treatment and imaging the following day. Before drug treatment, the cells were labeled with 0.1 μM Janelia Fluor (JF) 549 Halo dye for 30 min. Then, the media was replaced with FluoroBrite DMEM Complete Medium (Gibco, A1896701) supplemented with 10% fetal bovine serum (FBS; Gibco, 26140079), 2 mM GlutaMAX-I (Gibco, 35050061), 1x NEAA (Gibco, 11140050). Airyscan live-cell images of individual cells were taken pretreatment, 15min, 30min, and 45min after 1% 1,6-hexandiol (Sigma-Aldrich, 88571) and DMSO (Corning, 01023017) treatment.

UOK342 eGFP-TEAD1 stable cell line was plated into 8-well chambered cover glass (Cellvis, C8-1.5H-N) for FRAP experiment. Fluorescence bleaching was done on nuclear TEAD1 foci using bleach mode in Zen software. The region of interest was selected on either the entire condensates or part of it using a rectangular box of approximately 1μm x 1μm in half-FRAP and

2μm x 2μm in full-FRAP. At least twenty iterations of bleaching were done with a 488nm Argon laser at 100% power. ~140 rounds of imaging were performed before and after bleaching until fluorescence signal plateau, respectively, with an interval of 410ms. The $t_{1/2}$ was calculated using frapplot in R[79], with fit formula for one diffusion component.

**Western Blot**

Cells were seeded on 6-well culture plates (FALCON, 353046), and plasmid transfection using Lipofectamine 3000 was done the day before cell lysis. After 20 hours of transfection, cells were washed ice-cold PBS, then add 100uL of lysis buffer (50mM Tris-HCl pH=8, 100nM NaCl, 1% IGEPAL, 0.5% Sodium deoxycholate) with 1X protease inhibitor (cOmplete™, Mini, EDTA-free Protease Inhibitor Cocktail). Cells were allowed to lyse on ice for 20 min and collect supernatant after centrifugation at 21,000 x g for 30 min at 4°C. Lysis was later added 1X loading buffer (10% glycerol, 2% SDS, 0.05M Tris-HCl pH=6.4, 0.01M 2-Mercaptoethanol, 0.6% bromophenol blue), and denatured at 90°C for 10 mins. 10uL mixture was later added to SurePAGE™ 4-12% Bis-Tris gels (GenScript, #M00654). Protein was transferred to nitrocellulose membrane (LICOR, P/N 926-31090) by wet transfer, and blocked with 5% non-fat milk in TBS buffer. Membrane was incubated overnight at 4°C with 5% non-fat milk in TBS-T milk with primary antibodies 1:1000 anti-TEAD1, 1:1000 anti-GFP (Thermo Fisher, XH352366), 1:20,000 anti-β-actin (ABClonal, 3500100011). After washing in TBS-T, membranes were incubated at room temperatures for 1 h with IRdye 800CW Donkey anti-mouse (LICOR ,926-32212) and IRdye 680RD goat anti-rabbit secondary antibodies (LiCOR, 926-68071). Protein amounts were detected via LICOR Odyssey® M Imagers. Bands were quantified using FIJI.

**RT-qPCR and RNA-sequencing**

Total RNA was isolated from HK2 and UOK cells lines using the Direct-zol RNA MiniPrep kit (cat. no. R2052) and converted to complementary DNA using the Thermo Fisher High-Capacity

RNA-to-cDNA reverse transcription kit (cat. no. 4387406). The RT-qPCR was carried out on a QuantStudio 3 Real-Time PCR Instrument using PowerUp SYBR Green Master Mix (Thermo Fisher, cat. no. A25742). The following primers were used: Gapdh, 5′-CTCCTGCACCACCAACTGCT-3′ (forward) and 5′GGGCCATCCACAGTCTTCTG-3′ (reverse); TEAD1, 5′-GGACAGGCAAGACGAGGA-3′ (forward), and 5′-AGTGGCCGAGACGATCTG-3′ (reverse). mRNA levels were normalized to those of GAPDH.

RNA extraction for RNA-sequencing is performed similarly. RNA-seq was performed as a service at Novogene. In brief, mRNA samples were enriched using oligo(dT) beads and then used to prepare strand-specific cDNA libraries. Sequencing was done on Illumina Novaseq PE150. Individual reads are mapped to human genome hg38 by Hisat 2 v2.0.5. Featurecount in Rsubread was used to quantify gene expression level, and DESeq2Rpackage is used for differential expression analysis. Gene Ontology (GO) enrichment analysis of differentially expressed genes was used using DAVID[80].

**ChIP-sequencing**

Chromatin immunoprecipitation (Ch-IP) was performed based on previous studies[81]. In general, $10^8$ cells are used per each ChIP-seq experiment. HK2 and UOK cells were first treated with 1% formaldehyde in UOK media, followed by the addition of 0.125M glycine to halt cross-linking. The cells, washed in ice-cold PBS, were then lysed in cell lysis buffer, with subsequent nutation at 4°C. Cells were treated by dounce homogenization on ice, followed by centrifuge at 500 x g for 10min. The supernatant was discarded, and the pellets was resuspended using nuclear lysis buffer. Nuclear lysates were then sheared by Covaris E220 to achieve average chromatin length of 300-400 bp. The protein/chromatin complexes are captured using antibodies specific to the TEAD1, H3K9me3, YAP1, H3K27ac, and mouse IgG, and the mixtures were incubated overnight on nutator at 4°C. The antibody/chromatin complexes were later captured by magnetic protein G beads and the washed and eluted antibody/chromatin complex using elusion

buffer. After reversal of formaldehyde cross-linkes, DNA was purified with ChIP DNA Clean & Concentrator™ (ZYMO research, D5205) and library preparation was performed using NEBNext® Multiplex Oligos for Illumima® (NEB, 10129566).

ChIP-seq data were processed using the following pipeline. Raw sequencing reads in FASTQ format were quality-checked using FastQC. Reads were aligned to the human reference genome (hg38) using Bowtie2 (v2.3.5.3). The resulting BAM files were used to generate coverage tracks (bigWig format) using *bamCoverage* from the *deepTools* suite, without additional normalization. Gene tracks are visualized using IGV 2.16.2. Biological replicates (n = 2 per condition) were merged prior to peak calling. Peaks for TEAD1, YAP, and H3K27ac ChIP-seq were identified using MACS2 with default narrow peak settings and corresponding input controls used to reduce background signal. A false discovery rate (FDR) cutoff of $q < 0.01$ was applied for peak selection. To identify putative co-regulatory TEAD1/YAP regions, overlapping peaks between TEAD1 and YAP datasets were identified using the *bedintersect* function in BEDTools. The resulting intersected peak regions were used for motif enrichment analysis via MEME-ChIP from the MEME Suite. Gene Ontology (GO) enrichment analysis of intersected peak regions was done using DAVID [80].

To investigate the genomic context of TEAD1 foci, we performed ChIP-seq for H3K9me3 using the same protocol described above. *SICER2* [50] was used for peak calling to identify broad enrichment regions characteristic of H3K9me3-marked heterochromatin. To identify potential TEAD1 foci-associated binding sites, we used the intersect function in BEDTools to determine regions co-occupied by TEAD1 and H3K9me3. To compare these co-bound regions across cell lines, we employed *deepTools*[82] *computeMatrix* to quantify signal intensity at TEAD1 binding across all four cell lines. Heatmaps of TEAD1 signal were generated using *plotHeatmap* to visualize TEAD1 binding profiles in each cell line in TEAD1/H3K9me3 co-bound regions in foci-positive cell lines (UOK121 and UOK342).

**Binding and Expression Target Analysis (BETA)**

To evaluate the regulatory function of TEAD1, we performed Binding and Expression Target Analysis using the BETA basic module[52]. ChIP-seq peak regions for TEAD1 were used as input along with RNA-seq differential expression results from UOK121 and UOK342 cells. Differentially expressed genes were identified based on $\log_2$ fold change thresholds, and categorized as upregulated, downregulated, or unchanged. The distance between TEAD1 peaks and target genes was defined using regions identified by the intersection of TEAD1 and H3K9me3 ChIP-seq peaks (via BEDtools), reflecting chromatin context-specific binding. BETA computed regulatory potential scores for each gene based on binding site proximity and density and assessed whether TEAD1 functions primarily as an activator or repressor using a Kolmogorov–Smirnov (KS) test to compare cumulative distributions of gene categories.

**Proximity-based proteomics experiments**

**IF confirmation of biotinylation of TEAD1 foci components**

Cells were plated on glass coverslips in a 24-well plate and transfected the next day at 70% confluency using lipofectamine 3000 Transfection reagent (L3000015; ThermoFisher), followed by 24-hour incubation. To image nuclear localization of the construct miniTurbo-TEAD1-HaloTag, cells were stained with JF646-HaloTag ligand (100nM; Janelia Materials) for 30 min before fixation. Cells were treated with 500μM Biotin in fresh growth media for 10 min at 37˚C. Immediately after incubation, cell were washed with ice-cold DPBS for three times and fixed with 4% paraformaldehyde in PBS for 15 min on ice, permeabilized with ice-cold methanol at -20˚C for 5 min, and blocked with 1% wt/v BSA in DPBS at 4˚C for 30min. Primary antibodies against TEAD1(610923; BD Biosciences) was incubated overnight at 4˚C. Cells were then incubated with secondary antibody Alexa Fluor 488 Goat anti-mouse IgG (H+L) (a11001, ThermoFisher). Biotinylated proteins were stained using streptavidin-Alexa Fluor 568 (S11226; ThermoFisher) for 1hr at room temperature. The cells were then incubated with Hoecht 33342 at RT for 5 min and

mounted on glass slides with Vestashield and sealed with nail polish. Images were Airyscan-processed with the 1071 Zeiss Zen software (standard, 2D processing).

**Confirmation of protein biotinylation using Western Blot.**

Cells were plated on 10cm Petri dishes and transfected the next day at 70% confluency using lipofectamine 3000 Transfection reagent (L3000015; ThermoFisher), followed by 24-hour incubation. Cells were treated with 500μM Biotin in fresh growth medium for 10min at 37˚C, washed with ice-cold DPBS for three times, and collected using cell scrapers and centrifuged at 300xg, 4˚C for 5 min. Whole cell lysates were collected in 400μl RIPA buffer containing 50 mM Tris pH 8 (T60050-1000.0, Research Products International), 140 mM NaCl (S23025-3000.0, Research Products International), 1% Igepal® CA-630 (56741-50ML-F, Sigma Aldrich), 0.1% Sodium deoxycholate (30970-25G, Sigma Aldrich), 0.1% w/v sodium dodecyl sulfate (SDS, L3771, Sigma-Aldrich), and cOmplete™ Mini Protease Inhibitor Cocktail (11836170001, Sigma Aldrich) for 20 min on ice and clarified by centrifugation at 13,000 xg, 4˚C for 10min. The protein concentrations were measured by BCA assay. 175μg of proteins from the lysates were enriched for biotinylation using Pierce Streptavidin Magnetic beads (88816; ThermoFisher) and incubated overnight at 4˚C on a rotator. The bead slurry was washed twice with RIPA buffer, once with 1.0M KCL, once with 50mM TEAB buffer, and twice with RIPA buffer. About 10μg of proteins from Input, Post IP supernatant and pulldown samples were loaded on to the gel for immunoblotting. Biotinylated proteins were stained using Streptavitin-IRDye680 (926-68079; LICOR). Other antibodies used were anti-TEAD1 antibody (610923; DB Biosciences), and anti-β-actin antibodies (AC004; ABClonal).

**Sample preparation of proteomic analysis with miniTurbo:**

UOK342 cell stably expressing miniTurbo-TEAD1-HaloTag and miniTurbo-TEAD1 H3Mut-HaloTag were cultured overnight in 15cm Petri dishes and treated with 500μM Biotin for 10min at 37˚C. Cells were collected and lysed in 800μl RIPA buffer as described previously.

**TCA/Acetone Precipitation.** Cell lysates were buffered to pH 8.0 with 100mM Triethylammonium bicarbonate (TEAB) in 1.5 ml centrifuge tubes, then reduced using 25 ul of 50mM dithiothreitol for 1 hr. at 60 C. Samples were chilled on ice then alkylated using 25 ul of 50mM iodoacetamide for 15 minutes in the dark. Samples were then diluted on ice in 8x volume of 10% trichloroacetic acid in acetone w/v stored at -20 C. Samples were vortexed and incubated for at least 4 hours at -20 C. Samples were then pelleted by centrifugation at 16,000g for 10 minutes at 0 C. The supernatant was carefully removed leaving the pelleted protein on the walls of the tube. 500ul of neat acetone stored at -20 C. was added to the pelleted protein and vortexed. This was then incubated for at least 10 minutes at -20 C. before centrifugation at 16,000g once again and the supernatant carefully removed. The remaining acetone was allowed to evaporate for 10 minutes before addition of trypsin (Pierce) in 100mM TEAB at a ratio of 1/50 enzyme to protein and allowed to digest overnight at 37C. Digested peptides were lyophilized and re-constituted in 500μl RIPA buffer and incubated with 50μl Pierce Streptavidin Magnetic beads overnight at 4˚C on a rotator. The bead slurry was washed as described in WB confirmation followed by two times washes with ultrapure water. The washed beads were air-dried at 4˚C for 6 hr and stored at -20˚C.

**Eluting peptides from streptavidin linked magnetic beads.** Biotinylated peptides bound to streptavidin linked magnetic beads were separated from the final wash buffer by placing the Eppendorf tubes on a magnetic holder. After removing and setting aside the final wash buffer, the following steps were performed in the fume hood. Neat HFIP (200ul Millipore/Sigma Cat#105228) was added to each tube and put on a shaker at 1000 rpm for 10 minutes. The bead slurry was then placed on a magnetic holder to recover the HFIP eluted peptides from the magnetic beads.

HFIP extraction was performed twice and both peptide elutions were combined in a new Eppendorf tube. The combined extractions were evaporated to dryness in a speedvac and resuspended in 0.1% TFA. Samples were buffer exchanged using an Oasis HLB (Waters, Milford MA) with two washes of 0.1% TFA and eluted with 0.1% TFA, 60% acetonitrile into new tubes and dried by vacuum centrifugation prior to mass spectrometry analysis.

**Mass Spectrometry analysis:**

Tryptic peptides were analyzed by reverse-phase chromatography tandem mass spectrometry on a Vantage NEO UPLC interfaced with an Orbitrap Exploris 480 mass spectrometer (Thermo Fisher Scientific). Peptides were separated using a 2%–90% acetonitrile in 0.1% formic acid gradient over 90 min at 300 nl/min using an in-house packed 75-um ID x 15 cm column packed with ReproSIL-Pur-120-C18-AQ (2.4 µm, 120 Å bulk phase, Dr. Maisch). Survey scans of precursor ions were acquired from 375-1500 m/z at a resolution setting of 120,000. Precursor ions were isolated in data dependent mode with a 3 second cycle time using a 1.5 dalton isolation width and a 45s dynamic exclusion. Peptides were fragmented at a normalized HCD collision energy of 30 with a resolution setting of 30,000.

**Data analysis and candidate protein selection:**

Mass Spec data for all 6 files were processed together using Proteome Discoverer v3.1.1.93 (ThermoFisher Scientific) using Sequest with Match Between Runs enabled against the UniProt Homo sapiens database. The TEAD constructs were inserted at the end of the Human FASTA file. Search criteria included trypsin as the enzyme with two allowed missed cleavages, a 10-ppm precursor mass tolerance and a 0.02 Da fragment mass tolerance. Modifications included fixed carbamidomethylation on C, oxidation on M, deamidation on N or Q and biotin on K as variable modifications. Peptide identifications were filtered at the 1% FDR level using the Percolator Node in Proteome Discoverer. To facilitate candidate protein identification, peptide groups with biotin-tag were selected and analyzed non-quantitatively. Biotin-Peptide identified in

at least two out of three replicates in either WT or H3Mut is filtered for potential candidates. Unique peptides found in at least two out of three replicates of WT but not in H3Mut group were included in the candidate protein list. Venn diagram was generated based on the unique and shared proteins in WT and H3Mut.

Analysis of raw files were performed using Thermo Proteomic discover 3.1 software, using default settings with label-free quantification option enabled. The abundance values of biotin-peptides are normalized based on the median abundance of the all the peptides within the sample. Missing values in the replicates are adjusted through data imputation[83]. Abundance ratio and Adjusted p-Values are generated and visualized by volcano plot showing differentially enriched proteins. Proteins with biotin-peptides were filtered as mandatory criteria, proteins with >2 fold-enrichment compared to H3Mut were included in the candidate protein list in addition to the ones identified non-quantitatively as described above. String Analysis was generated based on the pulled candidate list. Protein-protein interaction networks and GO enrichment were rendered with settings at medium confidence (0.400).

**Reference:**


1 Banani, S. F., Lee, H. O., Hyman, A. A. & Rosen, M. K. Biomolecular condensates: organizers of cellular biochemistry. *Nat Rev Mol Cell Biol* **18**, 285-298 (2017). https://doi.org/10.1038/nrm.2017.7

2 Shin, Y. & Brangwynne, C. P. Liquid phase condensation in cell physiology and disease. *Science* **357** (2017). https://doi.org/10.1126/science.aaf4382

3 Mittag, T. & Pappu, R. V. A conceptual framework for understanding phase separation and addressing open questions and challenges. *Molecular Cell* **82**, 2201-2214 (2022). https://doi.org/https://doi.org/10.1016/j.molcel.2022.05.018

4 Lu, Y. *et al.* Phase separation of TAZ compartmentalizes the transcription machinery to promote gene expression. *Nat Cell Biol* **22**, 453-464 (2020). https://doi.org/10.1038/s41556-020-0485-0

5 Demmerle, J., Hao, S. & Cai, D. Transcriptional condensates and phase separation: condensing information across scales and mechanisms. *Nucleus* **14**, 2213551 (2023). https://doi.org/10.1080/19491034.2023.2213551

6 Hnisz, D., Shrinivas, K., Young, R. A., Chakraborty, A. K. & Sharp, P. A. A Phase Separation Model for Transcriptional Control. *Cell* **169**, 13-23 (2017). https://doi.org/10.1016/j.cell.2017.02.007

7 Boija, A. *et al.* Transcription Factors Activate Genes through the Phase-Separation Capacity of Their Activation Domains. *Cell* **175**, 1842-+ (2018). https://doi.org/10.1016/j.cell.2018.10.042

8 Muzzopappa, F. *et al.* Detecting and quantifying liquid-liquid phase separation in living cells by model-free calibrated half-bleaching. *Nat Commun* **13**, 7787 (2022). https://doi.org/10.1038/s41467-022-35430-y

9 McSwiggen, D. T. *et al.* Evidence for DNA-mediated nuclear compartmentalization distinct from phase separation. *Elife* **8** (2019). https://doi.org/10.7554/eLife.47098

10 Cai, D. *et al.* Phase separation of YAP reorganizes genome topology for long-term YAP target gene expression. *Nat Cell Biol* **21**, 1578-1589 (2019). https://doi.org/10.1038/s41556-019-0433-z

11 Sabari, B. R. *et al.* Coactivator condensation at super-enhancers links phase separation and gene control. *Science* **361** (2018). https://doi.org/10.1126/science.aar3958

12 Cho, W. K. *et al.* Mediator and RNA polymerase II clusters associate in transcription-dependent condensates. *Science* **361**, 412-415 (2018). https://doi.org/10.1126/science.aar4199

13 Chong, S. *et al.* Tuning levels of low-complexity domain interactions to modulate endogenous oncogenic transcription. *Mol Cell* **82**, 2084-2097 e2085 (2022). https://doi.org/10.1016/j.molcel.2022.04.007

14 Song, L. *et al.* Hotspot mutations in the structured ENL YEATS domain link aberrant transcriptional condensates and cancer. *Mol Cell* **82**, 4080-4098 e4012 (2022). https://doi.org/10.1016/j.molcel.2022.09.034

15 Cai, D. F., Liu, Z. & Lippincott-Schwartz, J. Biomolecular Condensates and Their Links to Cancer Progression. *Trends in Biochemical Sciences* **46**, 535-549 (2021). https://doi.org/10.1016/j.tibs.2021.01.002

16 Spannl, S., Tereshchenko, M., Mastromarco, G. J., Ihn, S. J. & Lee, H. O. Biomolecular condensates in neurodegeneration and cancer. *Traffic* **20**, 890-911 (2019). https://doi.org/10.1111/tra.12704

17 Linehan, W. M. The Genetic Basis of Kidney Cancer: Implications for Management and Use of Targeted Therapeutic Approaches. *European Urology* **61**, 896-898 (2012). https://doi.org/10.1016/j.eururo.2012.02.022

18 Linehan, W. M. & Ricketts, C. J. The Cancer Genome Atlas of renal cell carcinoma: findings and clinical implications. *Nat Rev Urol* **16**, 539-552 (2019). https://doi.org/10.1038/s41585-019-0211-5
19 Zheng, Y. & Pan, D. The Hippo Signaling Pathway in Development and Disease. *Dev Cell* **50**, 264-282 (2019). https://doi.org/10.1016/j.devcel.2019.06.003
20 Fu, M. *et al.* The Hippo signalling pathway and its implications in human health and diseases. *Signal Transduct Target Ther* **7**, 376 (2022). https://doi.org/10.1038/s41392-022-01191-9
21 Dong, J. *et al.* Elucidation of a universal size-control mechanism in Drosophila and mammals. *Cell* **130**, 1120-1133 (2007). https://doi.org/10.1016/j.cell.2007.07.019
22 Zhao, B. *et al.* Inactivation of YAP oncoprotein by the Hippo pathway is involved in cell contact inhibition and tissue growth control. *Genes & Development* **21**, 2747-2761 (2007). https://doi.org/10.1101/gad.1602907
23 Lei, Q. Y. *et al.* TAZ promotes cell proliferation and epithelial-mesenchymal transition and is inhibited by the hippo pathway. *Molecular and Cellular Biology* **28**, 2426-2436 (2008). https://doi.org/10.1128/Mcb.01874-07
24 Sourbier, C. *et al.* Targeting loss of the Hippo signaling pathway in NF2-deficient papillary kidney cancers. *Oncotarget* **9**, 10723-10733 (2018). https://doi.org/10.18632/oncotarget.24112
25 Harvey, K. F., Zhang, X. & Thomas, D. M. The Hippo pathway and human cancer. *Nat Rev Cancer* **13**, 246-257 (2013). https://doi.org/10.1038/nrc3458
26 Hao, S. *et al.* YAP condensates are highly organized hubs. *iScience* **27** (2024). https://doi.org/10.1016/j.isci.2024.109927
27 Wang, L. *et al.* Multiphase coalescence mediates Hippo pathway activation. *Cell* **185**, 4376-4393 e4318 (2022). https://doi.org/10.1016/j.cell.2022.09.036
28 Bonello, T. T. *et al.* Phase separation of Hippo signalling complexes. *EMBO J* **42**, e112863 (2023). https://doi.org/10.15252/embj.2022112863
29 Anglard, P. *et al.* Molecular and cellular characterization of human renal cell carcinoma cell lines. *Cancer Res* **52**, 348-356 (1992).
30 Hao, S. *et al.* YAP condensates are highly organized hubs. *iScience*, 109927 (2024).
31 Boeynaems, S. *et al.* Protein Phase Separation: A New Phase in Cell Biology. *Trends Cell Biol.* **28**, 420-435 (2018). https://doi.org/10.1016/j.tcb.2018.02.004
32 Roeder, R. G. & Rutter, W. J. Multiple forms of DNA-dependent RNA polymerase in eukaryotic organisms. *Nature* **224**, 234-237 (1969). https://doi.org/10.1038/224234a0
33 Creyghton, M. P. *et al.* Histone H3K27ac separates active from poised enhancers and predicts developmental state. *Proc Natl Acad Sci U S A* **107**, 21931-21936 (2010). https://doi.org/10.1073/pnas.1016071107
34 Shi, J. & Vakoc, C. R. The mechanisms behind the therapeutic activity of BET bromodomain inhibition. *Mol Cell* **54**, 728-736 (2014). https://doi.org/10.1016/j.molcel.2014.05.016
35 Hnisz, D. *et al.* Super-enhancers in the control of cell identity and disease. *Cell* **155**, 934-947 (2013). https://doi.org/10.1016/j.cell.2013.09.053
36 Kouzarides, T. Chromatin modifications and their function. *Cell* **128**, 693-705 (2007). https://doi.org/10.1016/j.cell.2007.02.005
37 Eissenberg, J. C. & Elgin, S. C. HP1a: a structural chromosomal protein regulating transcription. *Trends Genet* **30**, 103-110 (2014). https://doi.org/10.1016/j.tig.2014.01.002
38 Verdaasdonk, J. S. & Bloom, K. Centromeres: unique chromatin structures that drive chromosome segregation. *Nature Reviews Molecular Cell Biology* **12**, 320-332 (2011). https://doi.org/10.1038/nrm3107
39 Hall, L. E., Mitchell, S. E. & O'Neill, R. J. Pericentric and centromeric transcription: a perfect balance required. *Chromosome Research* **20**, 535-546 (2012). https://doi.org/10.1007/s10577-012-9297-9

40 de Lange, T. Shelterin: the protein complex that shapes and safeguards human telomeres. *Genes & Development* **19**, 2100-2110 (2005). https://doi.org/10.1101/gad.1346005
41 Anbanandam, A. *et al.* Insights into transcription enhancer factor 1 (TEF-1) activity from the solution structure of the TEA domain. *Proc Natl Acad Sci U S A* **103**, 17225-17230 (2006). https://doi.org/10.1073/pnas.0607171103
42 Hwang, J. J., Chambon, P. & Davidson, I. Characterization of the transcription activation function and the DNA binding domain of transcriptional enhancer factor-1. *EMBO J* **12**, 2337-2348 (1993). https://doi.org/10.1002/j.1460-2075.1993.tb05888.x
43 Magico, A. C. & Bell, J. B. Identification of a classical bipartite nuclear localization signal in the Drosophila TEA/ATTS protein scalloped. *PLoS One* **6**, e21431 (2011). https://doi.org/10.1371/journal.pone.0021431
44 Galli, G. G. *et al.* YAP Drives Growth by Controlling Transcriptional Pause Release from Dynamic Enhancers. *Mol Cell* **60**, 328-337 (2015). https://doi.org/10.1016/j.molcel.2015.09.001
45 Zhu, C. *et al.* A Non-canonical Role of YAP/TEAD Is Required for Activation of Estrogen-Regulated Enhancers in Breast Cancer. *Mol Cell* **75**, 791-806.e798 (2019). https://doi.org/10.1016/j.molcel.2019.06.010
46 Cebola, I. *et al.* TEAD and YAP regulate the enhancer network of human embryonic pancreatic progenitors. *Nature Cell Biology* **17**, 615-626 (2015). https://doi.org/10.1038/ncb3160
47 Farrance, I. K. G., Mar, J. H. & Ordahl, C. P. M-Cat Binding-Factor Is Related to the Sv40 Enhancer Binding-Factor, Tef-1. *Journal of Biological Chemistry* **267**, 17234-17240 (1992).
48 She, X. W. *et al.* The structure and evolution of centromeric transition regions within the human genome. *Nature* **430**, 857-864 (2004). https://doi.org/10.1038/nature02806
49 Ma, R. & Zhu, B. Pericentromeric sequences, where a conservation paradox occurs. *Trends Cell Biol* (2025). https://doi.org/10.1016/j.tcb.2025.01.011
50 Zang, C. *et al.* A clustering approach for identification of enriched domains from histone modification ChIP-Seq data. *Bioinformatics* **25**, 1952-1958 (2009). https://doi.org/10.1093/bioinformatics/btp340
51 Love, M. I., Huber, W. & Anders, S. Moderated estimation of fold change and dispersion for RNA-seq data with DESeq2. *Genome Biol* **15**, 550 (2014). https://doi.org/10.1186/s13059-014-0550-8
52 Wang, S. *et al.* Target analysis by integration of transcriptome and ChIP-seq data with BETA. *Nature Protocols* **8**, 2502-2515 (2013). https://doi.org/10.1038/nprot.2013.150
53 Branon, T. C. *et al.* Efficient proximity labeling in living cells and organisms with TurboID. *Nat Biotechnol* **36**, 880-887 (2018). https://doi.org/10.1038/nbt.4201
54 Cho, K. F. *et al.* Proximity labeling in mammalian cells with TurboID and split-TurboID. *Nat Protoc* **15**, 3971-3999 (2020). https://doi.org/10.1038/s41596-020-0399-0
55 Shin, S. *et al.* Super-resolution proximity labeling with enhanced direct identification of biotinylation sites. *Commun Biol* **7**, 554 (2024). https://doi.org/10.1038/s42003-024-06112-w
56 Minshull, J., Blow, J. J. & Hunt, T. Translation of cyclin mRNA is necessary for extracts of activated Xenopus eggs to enter mitosis. *Cell* **56**, 947-956 (1989). https://doi.org/https://doi.org/10.1016/0092-8674(89)90628-4
57 Lockhead, S. *et al.* The Apparent Requirement for Protein Synthesis during G2 Phase Is due to Checkpoint Activation. *Cell Reports* **32**, 107901 (2020). https://doi.org/https://doi.org/10.1016/j.celrep.2020.107901
58 Ochneva, A. *et al.* Protein Misfolding and Aggregation in the Brain: Common Pathogenetic Pathways in Neurodegenerative and Mental Disorders. *Int J Mol Sci* **23** (2022). https://doi.org/10.3390/ijms232214498
59 Jonkers, J. & Berns, A. Oncogene addiction: Sometimes a temporary slavery. *Cancer Cell* **6**, 535-538 (2004). https://doi.org/10.1016/j.ccr.2004.12.002

60 Serrano, M., Lin, A. W., McCurrach, M. E., Beach, D. & Lowe, S. W. Oncogenic ras provokes premature cell senescence associated with accumulation of p53 and p16INK4a. *Cell* **88**, 593-602 (1997). https://doi.org/10.1016/s0092-8674(00)81902-9
61 Mooi, W. J. & Peeper, D. S. Oncogene-induced cell senescence--halting on the road to cancer. *N Engl J Med* **355**, 1037-1046 (2006). https://doi.org/10.1056/NEJMra062285
62 Collado, M. & Serrano, M. Senescence in tumours: evidence from mice and humans. *Nat Rev Cancer* **10**, 51-57 (2010). https://doi.org/10.1038/nrc2772
63 Sun, T. & Chi, J. T. Regulation of ferroptosis in cancer cells by YAP/TAZ and Hippo pathways: The therapeutic implications. *Genes Dis* **8**, 241-249 (2021). https://doi.org/10.1016/j.gendis.2020.05.004
64 Magesh, S. & Cai, D. Roles of YAP/TAZ in ferroptosis. *Trends Cell Biol* **32**, 729-732 (2022). https://doi.org/10.1016/j.tcb.2022.05.005
65 Charlier, C., Lamaye, F., Thelen, N. & Thiry, M. Ultrastructural detection of nucleic acids within heat shock-induced perichromatin granules of HeLa cells by cytochemical and immunocytological methods. *Journal of Structural Biology* **166**, 329-336 (2009). https://doi.org/10.1016/j.jsb.2009.03.002
66 Jolly, C. *et al.* In vivo binding of active heat shock transcription factor 1 to human chromosome 9 heterochromatin during stress. *Journal of Cell Biology* **156**, 775-781 (2002). https://doi.org/10.1083/jcb.200109018
67 Biamonti, G. & Vourc'h, C. Nuclear stress bodies. *Cold Spring Harb Perspect Biol* **2**, a000695 (2010). https://doi.org/10.1101/cshperspect.a000695
68 Raff, J. W., Kellum, R. & Alberts, B. The Drosophila Gaga Transcription Factor Is Associated with Specific Regions of Heterochromatin Throughout the Cell-Cycle. *Embo Journal* **13**, 5977-5983 (1994). https://doi.org/DOI 10.1002/j.1460-2075.1994.tb06943.x
69 Bhat, K. M. *et al.* The GAGA factor is required in the early Drosophila embryo not only for transcriptional regulation but also for nuclear division. *Development* **122**, 1113-1124 (1996). https://doi.org/10.1242/dev.122.4.1113
70 Brown, K. E. *et al.* Association of transcriptionally silent genes with Ikaros complexes at centromeric heterochromatin. *Cell* **91**, 845-854 (1997). https://doi.org/Doi 10.1016/S0092-8674(00)80472-9
71 Klein, I. A. *et al.* Partitioning of cancer therapeutics in nuclear condensates. *Science* **368**, 1386-1392 (2020). https://doi.org/10.1126/science.aaz4427
72 Silva, J. L. *et al.* Targeting Biomolecular Condensation and Protein Aggregation against Cancer. *Chem Rev* **123**, 9094-9138 (2023). https://doi.org/10.1021/acs.chemrev.3c00131
73 Boija, A., Klein, I. A. & Young, R. A. Biomolecular Condensates and Cancer. *Cancer Cell* **39**, 174-192 (2021). https://doi.org/10.1016/j.ccell.2020.12.003
74 Kraus, F. *et al.* Quantitative 3D structured illumination microscopy of nuclear structures. *Nat Protoc* **12**, 1011-1028 (2017). https://doi.org/10.1038/nprot.2017.020
75 Sharifi-Sanjani, M., Meeker, A. K. & Mourkioti, F. Evaluation of telomere length in human cardiac tissues using cardiac quantitative FISH. *Nat Protoc* **12**, 1855-1870 (2017). https://doi.org/10.1038/nprot.2017.082
76 Schindelin, J. *et al.* Fiji: an open-source platform for biological-image analysis. *Nat Methods* **9**, 676-682 (2012). https://doi.org/10.1038/nmeth.2019
77 Bolte, S. & Cordelieres, F. P. A guided tour into subcellular colocalization analysis in light microscopy. *J Microsc* **224**, 213-232 (2006). https://doi.org/10.1111/j.1365-2818.2006.01706.x
78 Heck, N. *et al.* A new automated 3D detection of synaptic contacts reveals the formation of cortico-striatal synapses upon cocaine treatment in vivo. *Brain Struct Funct* **220**, 2953-2966 (2015). https://doi.org/10.1007/s00429-014-0837-2
79 Ding, G. (2019).

80 Sherman, B. T. *et al.* DAVID: a web server for functional enrichment analysis and functional annotation of gene lists (2021 update). *Nucleic Acids Res* **50**, W216-W221 (2022). https://doi.org/10.1093/nar/gkac194
81 O'Geen, H., Frietze, S. & Farnham, P. J. Using ChIP-seq technology to identify targets of zinc finger transcription factors. *Methods Mol Biol* **649**, 437-455 (2010). https://doi.org/10.1007/978-1-60761-753-2_27
82 Ramirez, F., Dundar, F., Diehl, S., Gruning, B. A. & Manke, T. deepTools: a flexible platform for exploring deep-sequencing data. *Nucleic Acids Res* **42**, W187-191 (2014). https://doi.org/10.1093/nar/gku365
83 Aguilan, J. T., Kulej, K. & Sidoli, S. Guide for protein fold change and p-value calculation for non-experts in proteomics. *Mol Omics* **16**, 573-582 (2020). https://doi.org/10.1039/d0mo00087f